

7:30–8:00 AM Coffee and Pastries—Grand Assembly

Cases of the Day

Moderator: Melissa L. Rosado de Christenson, MD

7:30–7:45 AM Case of the Day
Santiago Rossi, MD

7:45–8:00 AM Case of the Day
Cristopher A. Meyer, MD

New Horizons: Functional Imaging in the Chest

Moderator: Jeffrey R. Galvin, MD

8:00–8:40 AM Image-based Functional Measurements in the Chest
Eric A. Hoffman, PhD

8:40–9:05 AM Functional Imaging of the Lung and Quantitative Analysis Using Computed Tomography
Jonathan G. Goldin, MBChB, PhD

9:05–9:30 AM Functional MR Imaging of the Lung
Hiroto Hatabu, MD, PhD

9:30–9:55 AM Why and How Should Emphysema Be Quantified on CT?
Alexander A. Bankier, MD

9:55–10:15 AM Panel Discussion and Questions

10:15–10:30 AM Break

**STR NASCI Cardiovascular Symposium:
Ischemia and Imaging**

Moderator: Pamela K. Woodard, MD

10:30–10:50 AM The Role of Diagnostic Imaging in the Evaluation of Patients with Acute Chest Pain
Jack A. Ziffer, MD, PhD

10:50–11:10 AM Helical CT and Electron-Beam CT Imaging of Coronary Calcium: An Update
William Stanford, MD

11:10–11:30 AM Potential Role of MRI in Ischemic Heart Disease
Charles B. Higgins, MD

- 11:30–11:50 AM Cardiac Imaging with Multidetector-Row CT
Geoffrey D. Rubin, MD
- 11:50 AM–Noon Panel Discussion and Questions
- Noon–2:15 PM STR Lunch and Annual Business Meeting—Valencia

**Cardiovascular Symposium (continued):
The Heart and Associated Blood Vessels**

Moderator: Robert M. Steiner, MD

- 2:15–2:35 PM Cardiac Diagnosis: How to Approach the Chest Radiograph
Martin J. Lipton, MD
- 2:35–2:55 PM Teaching Cardiac and Great Vessel Anatomy with CT-derived 3D Reconstructions
Anna Rozenshtein, MD
- 2:55–3:15 PM MRI of Congenital Heart Disease
Gautham P. Reddy, MD
- 3:15–3:35 PM Pericardial Imaging
Lynn S. Broderick, MD
- 3:35–3:55 PM MR Imaging in Right Ventricular Dysplasia
Joel E. Fishman, MD, PhD
- 3:55–4:25 PM Imaging the Patient with Pulmonary Hypertension
Aletta Ann Frazier, MD, Robert M. Steiner, MD
- 4:25–4:50 PM Helical CT for Pulmonary Embolism: Current Status
Ella A. Kazerooni, MD
- 4:50–5:15 PM Panel Discussion and Questions

Benjamin Felson Memorial Lecture

Moderator: Jeffrey R. Galvin, MD

- 5:30–6:30 PM Information Management: PACS, Patient Data, and Diagnosis
Paul J. Chang, MD
- 6:30–8:00 PM Reception—Grand Lawn

Image-based Functional Measurements in the Chest

Eric A. Hoffman, PhD

At the time of publication, no abstract was available.

Disclosure Statement: Members of Marconi Medical Systems are co-investigators on our NIH-Bioengineering Partnership Grant.

Functional Imaging of the Lung and Quantitative Analysis Using Computed Tomography

Jonathan G. Goldin, MD, PhD

Department of Radiological Sciences

UCLA Medical Center

Introduction

Lung disease is a leading cause of mortality in the United States (2, 39). Chronic lung disease encompasses a spectrum of diffuse lung diseases including emphysema, chronic bronchitis, asthma, respiratory bronchitis, bronchiectasis, pulmonary thromboembolic disease and interstitial lung disease. CT, currently the best test to assess lung involvement in emphysema and interstitial lung disease, relies on abnormalities being detected when there is sufficient morphologic distortion to result in visually identified changes that occur relatively late in the pathogenesis of most disease processes. There is, however, poor correlation with the conventional measure of lung function and outcome. As a researcher highly respected in aspects of chronic obstructive lung disease recently reflected, “the simplicity of the lesion-holes in the lung, some (too-small) small airways, and bronchial gland enlargement, belies the functional and pathogenic complexity” (51). The same limitation likely applies to the reliance of visually evident parenchymal distortions in the CT images of patients with interstitial lung disease.

Radiologists, however, have been slow to go beyond the description of structural changes and provide quantitative measures of function. Further, what is needed is a method to distinguish the static and dynamic airway and parenchymal alterations exhibited in lung disease and to assess regional variations. High-resolution computed tomography is an established technique for the detailed evaluation of the pulmonary parenchyma and can characterize anatomic details of the lung as small as 200 to 300 μm , which corresponds to approximately the 7th to 9th generations of the airways and lung segments (27, 31, 36, 57). The addition of volume scanning allows data to be acquired through broad regions of interest during different phases of respiration or under different physiologic conditions providing critical insights into the relationships between structure and function (6, 7, 23). For quantitative image analysis to be useful and applied clinically it needs to be easy to perform, reproducible, observer independent and offer a valid measurement of disease presence and extent by comparison with physiologic or pathologic criteria. Further imaging protocols need to be tailored to

ensure the validity and reproducibility of the quantitative measures. The purpose of this chapter is to give an overview of quantitative techniques used and their application to various pulmonary diseases.

Imaging Protocols

The best imaging protocol for the quantitation of diffuse lung disease remains unresolved. With rapidly changing CT technology this remains an area of constant evolution. Currently, there is the need to choose, at the time of image acquisition, between sampling the lungs with high resolution thin sections at selected intervals and the use of a volume acquisition technique to acquire a 3-dimensional CT data set. The advantage of a rapidly acquired volumetric data set is that the images can be acquired in a single standardized breathhold and the lung is completely sampled allowing the creation of 3-dimensional models. Prior to the advent of subsecond multi-detector and spiral CT scanners, thick sections (5-10mm) were necessary to ensure a contiguous acquisition of the entire lung in the same breathhold. As a consequence, subtle abnormalities in the lung texture and density due to emphysema, lung fibrosis or air trapping were difficult to detect in the relatively large voxel sizes. For this reason, thin section sampling at intervals through the lung was preferentially chosen to allow detection of greater lung detail. However, with the advent of multi-detector scanners and subsecond scanning it is now possible to obtain full volume datasets in a single breathhold that can be reconstructed with true thin section resolution of the entire lung for the purpose of quantitative image analysis.

Standardization of the lung volume to either Total Lung Capacity (TLC), residual volume (RV) or a known lung volume in between the two at the time of scan acquisition is critical to ensure both the validity of quantitative measures and ensure reproducibility of measures on repeated studies. This is most accurately achieved with spirometric gating, in which the CT scan is triggered, and airflow mechanically inhibited, at a predetermined user selected level of breathhold (25). A similar technique using a pneumotachometer allows the patient to breathe between acquisitions and then upon return to a preselected inspiratory level scanning is initiated (24). It is also possible to obtain acceptably good reproducibility of lung volumes without the use of electronically gated CT scanners by the use of an incentive spirometer used during the time of scanning. The availability of commercial apparatus or spirometric gating or triggering is

scarce and, thus, most quantitative studies are performed without such methods. It is possible with volume acquisition techniques to confirm lung volume reproducibility without the need for spirometric gating (5) but this is only useful when the entire lung volume is acquired in a single breathhold and not when several high resolution images are obtained at intervals through the lungs.

In addition to volume triggered scanning, the ability to acquire or reconstruct images at 50-100 msec intervals, thus achieving real-time ciné sequences during the performance of respiratory maneuvers without compromise of image quality by motion, can also be useful (14, 17). Although the necessary technical parameters will vary according to the specific application, degree of resolution required, and anatomic region under examination, images of 1-3 mm collimation obtained between 300-500 msec intervals can be acquired as sequences that are triggered or simultaneously monitored by spirometry. ECG-gating may also be used to study the lower lobes free of cardiac motion artifacts (41). Similar results have been reported using Fast CT (sub-second Helical and multi-detector scanners). For most pulmonary functional applications, sequences acquired through the upper, mid and lower lungs provide an adequate sample of the lungs. By integrating the spirometric and imaging data, changes in lung attenuation for isolated regions of interest can be measured as a function of time, airflow, and lung volume (Figure 1).

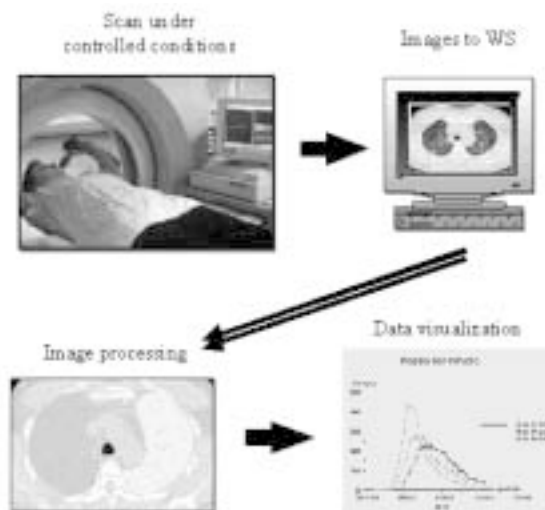


Figure 1: QIA is achieved by obtaining CT data at controlled, spirometrically gated lung volumes and transferring the data to automated analysis and display workstations.

Quantitative Image Analysis

The quantitative information obtained with HRCT may advance our understanding of pulmonary pathophysiology and offer insights into the potential mechanisms involved in the progression of lung disease (1, 15-18, 26, 28, 30, 35, 36-38, 40, 42-44, 45, 48, 50, 52-54, 58, 59, 61). Additional advantages of this technique are its non-invasive nature and ability to offer a comprehensive regional assessment not possible with conventional lung function tests. There has been an explosion in investigations to provide quantitative structural and functional information from digitally acquired image data. These methods include visual quantitation scoring systems, image display (such as multiplanar reformations, surface shading for 3D and volume rendering) (29, 40, 84), anatomic image quantitation (e.g., area and volume of airways and lungs) (1, 3, 4, 8, 10, 13, 17, 24, 37, 38, 59, 60) and regional characterization of lung tissue (analyzing attenuation, changes in attenuation and texture patterns in the imaged lung) (9, 12, 18, 52, 53, 56). Approaches to CT quantitation may be visual or computer aided.

Visual quantitation approaches utilize various scoring systems that categorize different parenchymal patterns and attempt to quantitate their extent and severity using an assessment of the amount of lung involved. In designing a visual scoring system it is important to separately score the extent of different CT patterns since these different patterns most likely have different functional effects. Such visual scoring CT systems have been developed for emphysema, idiopathic pulmonary fibrosis (IPF), scleroderma lung disease, and chronic PE. In most studies, this final score is calculated either by agreement between two reviewers at a joint reviewing session or by obtaining the mean of the reading scores for the two reviewers. For the most part, they are relatively subjective and lack reproducibility with larger inter- and intra-reader variation. Thus, attention has turned to computer-aided detection and quantitative techniques.

For computer aided techniques the anatomical components of the cardiopulmonary system need to be identified and segmented prior to quantitation. Several approaches and software packages have been developed to quantitatively assess the lung with varying degrees of complexity and overlap in functionality (Figure 2). These packages consist of varying sets of image segmentation and analysis tools written to answer specific thoracic clinical and research questions (11, 12, 32-34, 47, 53). Image segmentation is achieved using various combinations of threshold and knowledge based algorithms to identify the lung

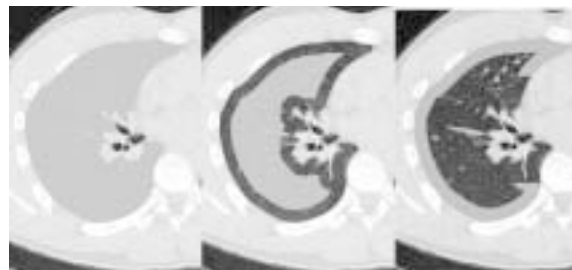


Figure 2: Automated knowledge based segmentation of lung parenchyma of (a) the entire right lung; (b) the central portion; and (c) the peripheral region.

and contained airways and blood vessels. For the most part the segmentation process is fully automated but allows manual correction if needed.

Three basic types of measurements are made on a segmented region of interest (ROI). The first category is measures relating to the size and shape of the ROI. The second category relates to attenuation (gray level) statistics and the third to image texture within the ROI. Much of the lung consists of intrathoracic gas which, when referenced to specific phases of respiration, can be used to assess parenchyma and airway integrity. An increase in either blood volume or in the interstitial, cellular or fluid content of the lung parenchyma results in increased attenuation of pixels relative to the low attenuation of air. Thus, measures that reflect changes in attenuation are indirect measures of these parenchymal changes as well (16, 30, 45). The greater the leftward shift of the "lung attenuation curve" (e.g., reflecting a greater proportion of pixels with low attenuation), the more extensive the lung destruction due to emphysema and/or expiratory airflow obstruction. Conversely a rightward shift of the curve (to a greater proportion of high attenuation) reflects an increase in either blood flow or in the interstitial, cellular, or fluid content of the lung parenchyma. By integrating spirometric and imaging data, changes in lung attenuation in defined regions of interest can be measured as a function of time (attenuation/time curves), airflow or lung volume. In addition, texture measurements quantify the nature of the local attenuation differences and take into account both the distance and direction of these differences (20, 21, 29, 49, 52, 54, 56). Measurements such as energy and entropy examine the overall homogeneity or heterogeneity of lung attenuation. Measurements such as autocorrelation and covariance may be derived from the second order histogram of lung density. Fractal analysis may also be applied to the analysis of the CT patents (46). Total and regional lung volumes can also be accurately calculated (8) (Figure 3).

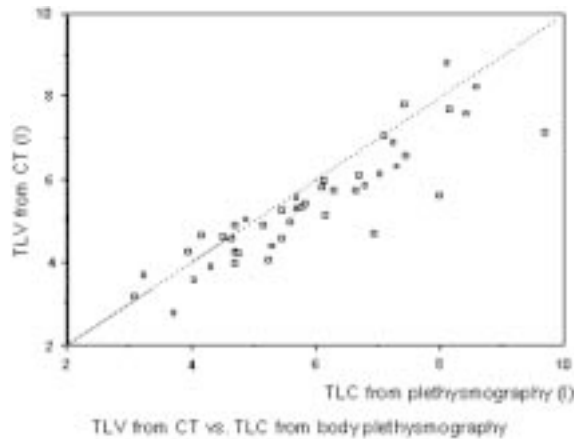


Figure 3: CT measurements of Total Lung Volume (TLV), acquired volumetrically at full inspiration to TLC, correlate extremely well ($r=0.98$) with Total Lung Capacity measured by body plethysmography.

Using computer-aided detection (CAD) techniques a computer system can be used to establish rules for recognition of image texture features such as normal parenchyma, bronchus, emphysema, ground glass attenuation and fibrosis (12) (Figure 4). The system can then be tested on a set of test images or ROI's. In a study by Delorme and colleagues this approach resulted in actual recognition of 70%-80% of patents in 1,889 five pixel by five pixel test regions (12). A similar approach, called the Adaptive Model Feature Method (AMFM), has been used by Uppaluri and colleagues to classify the images of patients with emphysema and lung fibrosis.

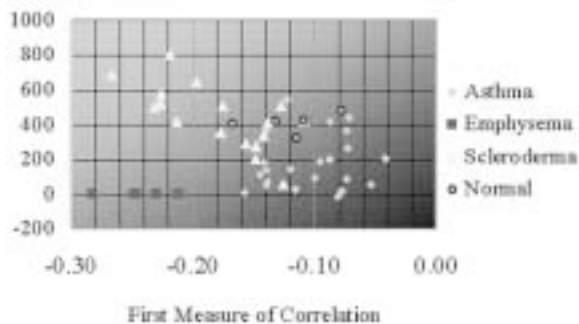


Figure 4: Lung texture measures allow for the detection of different lung structural changes as a consequence of parenchymal destruction (in emphysema), air trapping (in asthmatics) and alveolitis and fibrosis (in patients with scleroderma) as compared with normal lung structure (in well characterized normal subjects). Gradations of severity can also be determined by the relationship of the texture measures position relative to normal lung texture.

These techniques have been applied to distinguish: (a) normal and severely emphysematous patients on either a global basis (entire lung section) or regional basis (portion of lung section) (52); (b) healthy non-smokers, smokers and smokers with abnormal lung function (COPD) on either a global or regional basis (53); (c) airway reactivity and treatment response (17, 19); (d) other patient populations such as interstitial lung disease (i.e. IPF and sarcoidosis, asbestosis, and cystic fibrosis) (22, 56); and (e) areas of normal parenchyma, vessels, bronchi, emphysema, ground glass and lesions with intralobular fibrosis in HRCT images of patients with UIP (12). QIA can also be used as a measure of the efficacy of novel therapeutic techniques due to their ability to detect subtle regional variations not possible with conventional lung function tests (19).

REFERENCES

1. Adachi S, Kono M, Takemura T. Evaluation of 3D spiral CT bronchoscopy in patients with lung cancer. *Radiology* 1993; 189:264-269.
2. American Lung Association. Lung disease data. New York: American Lung Association; 1993.
3. Archer DC, Coblenz CL, deKemp R, Nahmias C, Norman G. Automated in vivo quantification of emphysema. *Radiology* 1993; 188:835-838.
4. Bae KT, Sloane RM, Gierada DS, Yusen RD, Cooper JD. Patients with emphysema: quantitative CT analysis before and after lung volume reduction surgery. *Radiology* 1997; 203:705-714.
5. Becker MD, Berkmen YM, Austin JH, et al. Lung volumes before and after lung volume reduction surgery: quantitative CT analysis. *Am J Respir Crit Care Med* 1998; 157(5 pt1):1593-1539.
6. Brown, RH; Mitzner, W; Zerhouni, E; Hirshman, CA. Direct in vivo visualization of bronchodilation induced by inhalational anesthesia using high-resolution computed tomography. *Anesthesiology* 1993; 78(2):295-300.
7. Brown, RH; Zerhouni, EA; Mitzner, W. Visualization of airway obstruction in vivo during pulmonary vascular engorgement and edema. *J Appl Physiol* 1995; 78(3):1070-1078.
8. Brown MS, McNitt-Gray MF, Mankovich NJ, Goldin JG, Aberle DR. Knowledge-based automated technique for measuring total lung volume from CT. *Proc. Society of Photo-Illumination Engineers (SPIE) Medical Imaging VIII* 1996; 2709:63-74.
9. Brown MS, Goldin JG, McNitt-Gray MF, Martin K, Sayre JW, Aberle DR. Automated assessment of split lung function for lung transplant patients. *Radiology* 1997; 205(P):395.
10. Brown MS, McNitt-Gray MF, Goldin JG, Aberle DR. Automated measurement of split and total lung volume from helical CT. *Radiology* 1997; 205(P):224.
11. Brown MS, McNitt-Gray MF, Goldin JG, Greaser LE, Aberle DR. Knowledge-based method for segmentation and quantitative analysis of lung function from CT. In: *Computer-Aided Diagnosis in Medical Imaging*, Doi K, MacMahon H, Giger ML, Hoffmann KR (eds.). *Proc 1st International Workshop on Computer-Aided Diagnosis*, Chicago, USA, 20-23 September, 1998.

12. Delorme S, Keller-Reichenbecher MA, Zuna I, et al. Usual interstitial pneumonia. Quantitative assessment of high-resolution computed tomography findings by computer-assisted texture-based image analysis. *Invest Radiol* 1997; 32(9):566-574.
13. Disler DG, Marr S, Rosenthal DI. Accuracy of volume measurements of computed tomography and magnetic resonance imaging phantoms by three-dimensional reconstruction and preliminary clinical application. *Invest Radiol* 1994; 29(8):739-745.
14. Genevois PA, Scillia P, de Maertelaer V, et al. The effects of age, sex, lung size, and hyperinflation on CT lung densitometry. *AJR* 1996; 167(5):1169-1173.
15. Goldin JG, Szold O, McNitt-Gray MF, Levine MS, Tashkin DP. Use of EBCT in the evaluation of patient's post single lung transplantation. *Am J Respir and Crit Care Med* 1995; 9(51):81.
16. Goldin JG, Aberle DR. Functional imaging of the airways. *J Thorac Imaging* 1997; 12:29-37.
17. Goldin JG, McNitt-Gray MF, Sorenson SM, et al. Airway hyperreactivity: assessment with helical thin-section CT. *Radiology* 1998; 208(2):321-329.
18. Goldin J, Brown MS, McNitt-Gray MF, Aberle DR. Automated assessment of split lung function in post lung transplant evaluation. *Proceedings of SPIE* 1998; 3337: 14-23.
19. Goldin JG, Tashkin DP, Kleerup EC, Greaser LE, Haywood UM, Sayre JW, Simmons MD, Suttorp M, Colice GL, Vandend Burgt J, Aberle DR. Comparative Effects of HFA—and CFC—Beclomethasone Dipropionate Inhalation on Small Airways: Assessment using Functional Helical Thin-Section Computed Tomography. *J Allergy Clin Immunol* 1999; 104(6):S258-267.
20. Haralick K, Shanmugan I, Dinstein. Textural features for image classification. *IEEE Trans Man Sys Cyber* 1973; SMC-3(6): 610-621.
21. Haralick K. Statistical and structural approaches to texture. *Proc IEEE* 1979; 67(5): 786-804.
22. Hartley PG, Galvin JR, Hunninghake GW, et al. High-resolution CT-derived measures of lung density are valid indexes of interstitial lung disease. *J Appl Physiol* 1994; 76(1):271-277.
23. Herold CJ, Brown RH, Mitzner W, et al. Assessment of pulmonary airway reactivity with high-resolution CT. *Radiology* 1991; 181(2):369-74.
24. Hoffman EA, McLennan G. Assessment of the pulmonary structure-function relationship and clinical outcomes measures: quantitative volumetric CT of the lung. *Acad Radiol* 1997; 4(1):758-776.
25. Kalender W, Rienmuller R, Seissler W, et al. Measurement of pulmonary parenchymal attenuation: use of spirometric gating with quantitative CT. *Radiology* 1990; 175:265-268.
26. Kaneko M, Ehuchi K, Ono R. Three-dimensional display of bronchial images by helical scanning CT. *Radiology* 1990; 177(P):174.
27. Klein J, Gamsu G. High-resolution computed tomography of diffuse lung disease. *Invest Radiol* 1989; 24:805-812.
28. Kramer SS, Hoffman EA. Physiologic imaging of the lung with volumetric high-resolution CT. *J Thorac Imaging* 1995; 10(4):280-290.
29. Laws. Textured Image Segmentation. USCIP technical report no 940; University of Southern California, 1980.
30. Lynch DA, Newell JD, Tschomper BA, Cink TM, Newman LA, Bethel R. Uncomplicated asthma in adults: comparison of CT appearance of the lungs in asthmatic and healthy subjects. *Radiology* 1993; 188:829-833.
31. Mathieson JR, Mayo JR, Staples CA, Muller NL. Chronic diffuse infiltrative lung disease: comparison of CT and chest radiography. *RadioGraphics* 1989; 171:111-116.
32. McNitt-Gray MF, Johnson TD, Aberle DR. TRIAD—a thoracic radiology image analysis and display workstation. *Med Physics* 1994; 21(6):905.
33. McNitt-Gray MF, Kimme-Smith C, Aberle DR. Calibration of airway area measurements from HRCT images of normal and asthmatic patients. *Med Physics* 1994; 21(6):926.
34. McNitt-Gray MF, Goldin JG, Johnson TD, Tashkin DP, Aberle DR. Development and testing of image processing methods for the quantitative assessment of airway hyperresponsiveness (AHR) from high-resolution CT images. *J Comput Assist Tomogr* 1997; 21(6):939-947.
35. Müller NL, Staples CA, Miller RR, Abboud RT. Density maps: an objective method to quantitative emphysema using computed tomography. *Chest* 1988; 94: 782-787.
36. Murata K, Itoh H, Todo G, et al. Centrilobular lesions of the lung: demonstration by high-resolution CT and pathologic correlation. *Radiology* 1986; 161:641-645.
37. Naidich DP, Webb WR, Müller NL. Thoracic computed tomography: current concepts. In: Potchen EJ, Grainger RG, Greene R, eds. *Pulmonary Radiology*. W.B. Saunders: Philadelphia, 1993:386-404.
38. Naidich DP. Volumetric scan change perceptions in thoracic imaging. *Diagn Imag* 1993; 4:70-74.
39. National Center for Health Statistics. Vital statistics for the United States, vol. 11: mortality, part A for delta years 1986-89. Washington, DC: Public Health Service; 1990.
40. Ney DR, Kuhlman JC, Hruban RH. Three-dimensional CT-volumetric reconstruction and display of the bronchial tree. *Invest Radiol* 1990; 25:736-742.
41. Okazawa M, Muller N, McNamara AE, et al. Human airway narrowing measured using high resolution computed tomography. *Am J Respir Crit Care Med* 1996; 154(5):1557-1562.
42. Reinhardt, JM; Hoffman, EA. Quantitative pulmonary imaging: spatial and temporal considerations in high-resolution CT. *Acad Radiol* 1998; 5(8):539-46.
43. Remy-Jardin M, Remy J, Deffontaines C, Duhamel A. Assessment of diffuse infiltrative lung disease: comparison of conventional CT and high-resolution CT. *Radiology* 1991; 181:157-162.
44. Remy-Jardin M, Remy J, Marquette CH, Wattinne L, Giraud F, Tonnel AB. Central airways in asthmatics and control subjects: evaluation with spirometric-gated spiral CT. *Radiology* 1992; 185(P):131.
45. Rienmüller R, Behr J, Kalender WA, et al. Standardization quantitative high-resolution CT in lung diseases. *J Comput Assist Tomogr* 1991; 15:742-749.
46. Rodriguez LH, Vargas PF, Raff U, et al. Automated discrimination and quantification of idiopathic pulmonary fibrosis from normal lung parenchyma using generalized fractal dimensions in high-resolution computed tomography images. *Acad Radiol* 1995; 2(1):10-18.
47. Rubin GD, Beaulieu CF, Argiro V, et al. Perspective volume rendering of CT and MR images: applications for endoscopic imaging. *Radiology* 1996; 199:321-330.

48. Schaefer CM, Prokop M, Zinh C. Spiral CT of the anastomotic complications after lung transplantation. *Radiology* 1993; 189(P):263.
49. Sonka M, Hlavac V, Boyle R. *Image Processing, Analysis and Vision*. Chapman and Hall computing: London 1993.
50. Swensen SJ, Aughenbaugh GL, Douglas WW, Myers JL. High resolution CT of the lungs: findings in various pulmonary diseases. *AJR* 1992; 158:971-979.
51. Thurlbeck WM. Emphysema then and now. *Can Respir J* 1994; 1:21-39.
52. Uppaluri R, Mitsa T, Sonka M, Hoffman EA, McLennan G. Quantification of pulmonary emphysema from lung computed tomography images. *Am J Respir Crit Care Med* 1997; 156(1):248-254.
53. Uppaluri R, McLennan G, Sonka M, Hoffman EA. Computer-based objective quantitative assessment of pulmonary parenchyma via x-ray CT. *Proc. SPIE Conference on Physiology and Function from Multidimensional Images* 1998; 3337:377-383.
54. Uppaluri R, McLennan G, Enright P, Standen JR, Boyer-Pfersdorf, Hoffman EA. Adaptive multiple feature method (AMFM) for the early detection of parenchymal pathology in a smoking population. *Proc. SPIE Conference on Physiology and Function from Multidimensional Images* 1998; 3337:8-13.
55. Uppaluri, R; Hoffman, EA; Sonka, M; Hartley, PG; Hunninghake, GW; McLennan, G. Computer recognition of regional lung disease patterns. *Am J Respir Crit Care Med* 1999; 160(2):648-654.
56. Uppaluri, R; Hoffman, EA; Sonka, M; Hunninghake, GW; McLennan, G. Interstitial lung disease: A quantitative study using the adaptive multiple feature method. *Am J Respir Crit Care Med* 1999; 159(2):519-525.
57. Webb WR. High-resolution CT of the lung parenchyma. *Radiol Clin North Am* 1989; 27:1085-1097.
58. Webb WR, Stern EJ, Kanth N, Gamsu G. Dynamic pulmonary CT: findings in healthy adult men. *Radiology* 1993; 186:117-124.
59. Wood SA, Hoford JD, Hoffman EA, Zerhouni E, Mitzner W. A method for measurement of cross sectional area, segment length, and branching angle of airway tree structures in situ. *Comp Med Imag Graph* 1995; 19(1):145-152.
60. Wu M, Chang J, Chiang A, Lu J, Hsu H, Hsu W, Yang C. Use of quantitative CT to predict postoperative lung function in patients with lung cancer. *Radiology* 1994; 191:257-262.
61. Zagers R, Vrooman HA, Aarts NJM, Stolk J, Schultze LJ, van Voorthuisen AE, Reiber JHC. Quantitative analysis of computed tomography scans of the lungs for the diagnosis of pulmonary emphysema: a validation study of a semiautomated contour detection technique. *Invest Radiol* 1995; 30(9):552-562.

Functional MR Imaging of the Lung

Hiroto Hatabu, M.D., Ph.D.

*Director of Pulmonary Functional Imaging Research, Associate Professor of Radiology
University of Pennsylvania Medical Center*

Recent development of fast MR imaging techniques opened a new window for functional assessment of the lung.[1] The newer generation MR scanner with its higher-strength gradient system and echo-planar capability can control the gradient very accurately and rapidly. The fast MR techniques, which are facilitated by the emergence of these new MR systems with enhanced gradient, are essential for the MR imaging of the lung. The difficulties in MR imaging of the lung have been posed by lung morphology and its physiological motion. The fast MR imaging techniques to overcome the problems of lung imaging including recent applications of fast MR techniques in pulmonary perfusion and ventilation imaging will be discussed.

Morphology and Physiology of the Lung and MR Signal

The lung has unusual morphological and physiological characteristics.[2] The human lung contains approximately 300 million anatomic alveoli measuring 200–300 microns in diameter, with a total surface area of 50–70 m². The overall density of the lung is 0.3 g/ml at end-expiration, and 0.15 g/ml at maximal inspiration. Minute ventilation at rest is about 6 L/min, and cardiac output from the right ventricle is about 5 L/min. This matching of ventilation with perfusion implies an intimate association between the gas spaces of the lung and pulmonary circulation. It is known that much of the hypoxemia and carbon dioxide retention observed in patients with various pulmonary diseases are caused by mismatching of ventilation and perfusion in the lung.[3] The alveoli have very thin walls because oxygen diffusion is particularly impeded by the low solubility of oxygen in water (0.03 ml/L; 20 times less than the solubility of carbon dioxide). The lung produces little MR signal, and appears dark on conventional MR sequences. The principal reason for poor MR signal from the lung is due to its unique alveolar architecture; namely the presence of multiple air / soft tissue interfaces. [4-6] The multiple interfaces of air and soft tissue result in very heterogeneous magnetic susceptibility, which produces large local gradients. The local gradients act to dephase the MR signal from the lung. (very short T₂* and T₂'). [7,8] Therefore, when conventional MR sequences are utilized, the MR signal from the lung decays extremely rapidly according

to T₂* time constant of about 1.4 ms before it is ever observed. [9,10]. In addition, other factors also contributing to the poor MR signal from the lung include relatively low proton density in the lung, and signal loss due to motion (cardiac and respiratory), pulmonary blood flow, and molecular diffusion. [4-8]

Fast MR Imaging of the Lung

The fundamental approach to acquiring signal from the lung, with its very short T₂*, is to acquire the signal before it decays, namely to sample the signal with minimal effective echo delay time (TE). Promising methods to accomplish this reduction in TE are [11]; 1) Reduced TE spin-echo (SE) imaging; 2) Projection reconstruction (PR) imaging; 3) Use of multiple RF refocusing pulses as utilized in the CPMG (Carr-Purcell-Meiboom-Gill) and fast SE imaging; 4) Gradient echo imaging with an ultra-short TE; 5) Single-shot fast SE or HASTE (half-Fourier single-shot fast SE) imaging.

Although historically interesting, improved methods of lung imaging emerged when fast MR imaging techniques such as gradient echo imaging with an ultra-short TE and single-shot fast SE imaging were made available. Multiple images are now acquired within a single breath-hold, dramatically decreasing the image blurring due to physiological respiratory motion.

Recently, a new technique to image the lung in vivo with complete coverage of both lungs in a single breath-hold has been reported using a multi-slice interleaved submillisecond TE gradient-echo sequence.[10,12] The method requires a high-speed, high-strength gradient system, and an optimized gradient-echo sequence to image lung with TE as short as 700 ms. The technique uses fractional echo sampling, high bandwidth data acquisition, and a truncated RF pulse to minimize TE. The signal from the normal lung parenchyma diminished exponentially with prolongation of TE. The measured T₂* in six normal volunteers ranged from 0.89 to 2.18 (1.43 ms ± 0.41 ms).

HASTE is a single-shot turboSE sequence where data are acquired during a train of 180° refocusing pulses. An echo spacing of 4.2 ms was used in this study and image reconstruction was performed with a half-Fourier method. The acquisition time for a 128 x 256 matrix was only 302 ms. The short echo spacing

made the pulse sequence relatively resistant to the inhomogeneous magnetic susceptibility of lung parenchyma, while the short data acquisition made the sequence insensitive to respiratory and cardiac motions. In patients with pulmonary disorders, the HASTE sequence demonstrated abnormalities of the lung parenchyma, including pulmonary edema, pulmonary hemorrhage, and bronchiectasis. This MRI technique might be utilized for the early detection of lung cancer or pulmonary metastasis in children, given the lack of ionizing radiation.[13,14]

Functional Imaging of the Lung

Fast MR imaging techniques with a very short TE are overcoming the problem of inhomogeneous magnetic susceptibility.[10,12] In addition, the single-shot fast SE sequence can now depict the lung parenchyma, providing a platform for MR imaging of the lung.[13,14]

Pulmonary perfusion can be assessed by the use of T1 weighted ultra-short TE sequence and contrast agents. [15] In an animal model, a perfusion defect due to a pulmonary embolus was clearly shown and confirmed by cine angiography. Based upon these investigations, we conclude that MRI of lung perfusion is feasible. Recent preliminary reports showed the feasibility of the MR perfusion technique in the evaluation of patients with pulmonary embolism [16] and unilateral lung transplantation.[17] This dynamic MR technique may also be used for the characterization of a single pulmonary nodule.[18] Another important application of the technique is the evaluation of pulmonary emphysema before lung volume reduction surgery. [19-21] Moreover, by fitting a portion of the time-intensity curve to a gamma variate function, flow parameters such as peak time, apparent mean transient time, and blood volume can be calculated[22]. The natural extension of this 2D technique is breath-hold contrast-enhanced 3D MR technique with short TR and TE.[23] With the implementation of a short TE of 2 ms, both pulmonary perfusion as well as the pulmonary vasculature were depicted in a 25-second breath-hold. Perfusion defects with accompanying obliteration of the regional pulmonary vasculature were demonstrated in both a porcine model and in patients with pulmonary embolism. Fast MR techniques also drastically advanced 3D contrast-enhanced MR angiography. Preliminary study in 30 patients with suspected pulmonary embolism demonstrated the feasibility of these techniques.[24]

Another approach for the evaluation of pulmonary perfusion we have devised is the modification of EPI-STAR sequence.[25] A modified fast gradient echo or single shot turbo spin-echo pulse sequence instead of echo planar imaging is utilized for image

acquisition, which is robust for magnetic susceptibility artifacts. Within each breath-holding period, two sets of images are acquired. In only one set of the images an RF pulse is applied to the right ventricle and main pulmonary artery in order to invert the magnetization of blood within those structures. After an inflow period (TI), which is on the order of a few hundred milliseconds to seconds, data are acquired using fast gradient echo or single-shot, half-Fourier, turbo spin-echo (HASTE) pulse sequences. The subtraction of the two images results in the perfusion image. [26-28] The merit of this technique lies in its potential to provide a non-invasive method for the absolute measurement of pulmonary perfusion by the application of a mathematical model. [28]

The assessment of regional ventilation in human lungs is important for the diagnosis and evaluation of a variety of pulmonary disorders including pulmonary emphysema, diffuse lung disease (i.e., sarcoidosis, pulmonary fibrosis), lung cancer, and pulmonary embolism. Oxygen modulates MR signals of blood and fluid through two different mechanisms; (1) a paramagnetic property of deoxyhemoglobin and (2) a paramagnetic property of molecular oxygen itself. [29,30] Molecular oxygen is weakly paramagnetic with a magnetic moment of 2.8 Bohr magnetons. [30,31] Young et al demonstrated reduction in T1 relaxation time of blood at 0.15 Tesla after inhalation of oxygen. [30,32] After inhalation of 100% oxygen, the concentration of dissolved oxygen in arterial blood increases by approximately five times.

Recently, we have demonstrated the feasibility of oxygen inhalation to evaluate regional pulmonary ventilation and examined the effect of oxygen inhalation on relaxation times in various tissues. [33,34] Signal changes from the right upper quarter portion of the right lung following alternate administration of 10L/min air (21% oxygen) and 100% oxygen via a mask are demonstrated. Calculated T1 values of the lung with various TIs before and after administration of oxygen were 1336 ± 46 ms and 1162 ± 33 ms, respectively. The observed change in T1 value confirms that molecular oxygen can be used as an effective T1 shortening agent in the assessment of ventilation in humans. Single-shot fast SE sequence was used to obtain MR signal from lung parenchyma, which has very short T2* value. The sequence is T1-weighted by the inversion recovery preparation pulse.

Laser-polarized Xe-129 and He-3 were proposed for ventilation MR imaging.[35-38] These noble gases can be hyperpolarized using optical pumping technique. MR signal from these noble gases may be increased by 100,000 times compared with the MR signal in a thermal equilibrium state. The strong

signal from the noble gases enable the acquisition of the data from gas itself. A preliminary clinical study by Kauczor et al demonstrated feasibility in assessing various pulmonary diseases including chronic obstructive lung disease, bronchiectasis, and lung cancer.[39,40] Diffusion of these noble gases impeded by alveolar structure can be measured. In addition, Xe-129 can be dissolved in blood, which may enable perfusion imaging as well as functional brain imaging.[41] Recent spectroscopic technique with Xe-129 demonstrated the possibility of separating the signal from lung parenchyma and blood.[42] Xe-129 may be injected intravenously for delivery to the lung and vasculature.[43] The hyperpolarized noble gas techniques provide new exciting applications.[44]

Although extremely promising, these agents are not ready for routine clinical use because of the high costs of noble gases and the apparatus for laser-polarization as well as the narcotic effects of large concentrations of inhaled noble gases. Any gases other than oxygen utilized for ventilation study, i.e., radioactive gases or hyperpolarized gases, are either heavier or lighter than oxygen. Therefore, the behavior of these gases may be different from oxygen in the lungs with gravitational effect.

The oxygen-enhanced MR ventilation technique utilizes conventional proton-based MR imaging. Oxygen is available in most MR units for patients and its administration is safe and inexpensive. Thus the oxygen-enhanced MRI technique for assessing pulmonary ventilation has the potential to provide a noninvasive means of assessing regional pulmonary ventilation at high resolution. Combined with the MRI perfusion studies, this technique has the potential to have a major impact on the diagnosis and assessment of a variety of pulmonary disorders.[45]

MR assessment of pulmonary ventilation-perfusion is possible when combined with recent first-pass contrast-enhanced MR perfusion technique using Gd-DTPA.[15,23,45,46] The combination of ventilation-perfusion techniques is particularly interesting when airway obstruction and pulmonary embolism, two classic disease models of the lung with contrasting radiographic manifestations are studied. Airway obstruction causes regional hypoxemia, which elicits hypoxic vasoconstriction, resulting in an accompanying decreased regional perfusion. Therefore, matched regional ventilation-perfusion deficit is expected when a combined ventilation-perfusion imaging study is performed. In contrast, pulmonary embolism does not cause airway obstruction. Therefore, regional perfusion deficit without ventilation deficit (mismatched ventilation-perfusion) is expected on the combined ventilation-perfusion imaging study. [45]

New Horizons: Future of MR Imaging of the Lung

MR ventilation-perfusion techniques have the potential to play an important part in 21st century pulmonary function testing. With the availability of high-resolution CT, why do we pursue the development of lung parenchymal imaging by MR? CT diagnosis is based on morphological findings as well as limited density information (calcium, fat, contrast enhancement). MR, on the other hand, has the potential for multi-parametric characterization of pathology based upon relaxation times, perfusion, ventilation, proton density (lung water determination), diffusion, susceptibility-induced T2* changes as reflections of alveolar architecture. Fast MR imaging is opening a new exciting window to multi-functional MR imaging of the lung. [1]

Quantification of pulmonary perfusion can be achieved by first-pass contrast agent technique or arterial spin labeling technique. The first-pass contrast agent method is easy to be applied, and provide pixel-by-pixel mapping of perfusion parameters. However, there are issues to be solved theoretically including deconvolution, leakage of contrast agent, and definition of output function. Arterial spin labeling technique is non-invasive and can be repeated. However, implementation and application are rather difficult.

Imaging of ventilation can be performed using hyperpolarized noble gas technique or oxygen-enhanced MR imaging. Both methods are relatively new and novel. Hyperpolarized noble gas technique demonstrates the flow of gas itself, while oxygen-enhanced MR imaging shows transfer of molecular oxygen indirectly through enhancement of protons in lungs by paramagnetic effect of molecular oxygen. The real premises of these methods are dynamic imaging of ventilation and physics-based approaches for analyses of dynamic imaging data.

The registration of quantified ventilation/perfusion images is crucial. However, the fact that ventilation requires motion of lung indeed proposes a fundamental challenge for registration of ventilation/perfusion images. At the same time, physics-based approach of registration of lung imaging provides a unique mathematical description of lung mechanics.

Ventilation, perfusion, and biomechanics are three major components of lung function. MR imaging provides a powerful tool for 21st century functional imaging of the lung.

Disclosure Statement: principal investigator, Phase I study MR assessment of lung ventilation, Nycomed-Amersham Co.

REFERENCES

- Hatabu H, Chen Q, Stock KW, Gefter WB, Itoh H. Fast MR imaging of the lung. *Eur J Radiol* 1999; 29:114-132.
- Albertine KH. Structural organization and quantitative morphology of the lung In Cuttillo AG (ed), *Application of Magnetic Resonance to the Study of Lung*. Armonk, NY, Futura Publishing Co, Inc, 1996: 73-114.
- West JB, Wagner PD. In: Crystal RG, Barnes PJ, West JB, Weibel ER, eds. *The lung scientific foundations*. Philadelphia: Lippincott-Raven, 1997, 1693-1709.
- Cuttillo AG, Ganesan K, Ailion DC, Morris AH, Durney CH, Symko SC, Christman RA. Alveolar air-tissue interface and nuclear magnetic resonance behavior of lung. *J Appl Physiol* 1991; 70:2145-2154.
- Ailion DC, Case TA, Blatter DD, Morris AH, Cuttillo AG, Durney CH, Johnson SA. Application of NMR spin imaging to the study of lungs. *Bull Magn Reson* 1984; 6:130-139.
- Case TA, Durney CH, Ailion DC, Cuttillo AG, Morris AH. A mathematical model of diamagnetic line broadening in lung tissue and similar heterogenous systems: calculations and measurements. *J Magn Reson* 1987; 73:304-314.
- Bergin CJ, Pauly JM, Macovski A. Lung parenchyma: Projection reconstruction MR imaging. *Radiology* 1991; 179:777-781.
- Bergin CJ, Glover GH, Pauly JM. Lung parenchyma: magnetic susceptibility in MR imaging. *Radiology* 1991; 180:845-848.
- Hatabu H, Alsop DC, Listerud J, Bonnet M, Gefter WB. T2* and proton density measurement of normal human lung parenchyma using submillisecond TE gradient echo MR imaging. *Eur J Radiol* 1999; 29:245-252.
- Hatabu H, Alsop D, Bonnet M, Listerud J, Pietra G, Gefter W. Approaches to MR imaging of lung parenchyma utilizing ultrashort TE gradient echo and fast SE sequences. *Proceedings, Society of Magnetic Resonance, Second Meeting*. San Francisco, August 6-12, 1994:1474.
- Gefter WB, Hatabu H, Hoffman EA, Ailion D, Cuttillo AG. *Magnetic Resonance in Experimental and Clinical Respiratory Medicine: State of the Art and Potential*. In Cuttillo AG (ed), *Application of Magnetic Resonance to the Study of Lung*. Armonk, NY, Futura Publishing Co, Inc, 1996: 503-538
- Alsop DC, Hatabu H, Bonnet M, Listerud J, Gefter W. Multi-slice, breathhold imaging of the lung with submillisecond echo times. *Magn Reson Med* 1995; 33:678-692.
- Hatabu H, Gaa J, Tadamura E, Li W, Garpestad E, Edelman RR. Lung parenchyma: MRI with a half-Fourier single-shot turbo SE (HASTE) sequence. *Proceedings, Society of Magnetic Resonance, Fourth Meeting*. New York, 1996:769.
- Hatabu H, Gaa J, Tadamura E, Stock KW, Garpestad E, Edelman RR. MR imaging of pulmonary parenchyma with a Half-Fourier Single-Shot TurboSE (HASTE) Sequence. *Eur J Radiol* 1999; 29:152-159.
- Hatabu H, Gaa J, Kim D, Li W, Prasad PV, Edelman RR. Pulmonary perfusion: qualitative assessment with dynamic contrast-enhanced MRI using ultra-short TE and inversion recovery turbo FLASH. *Magn. Reson. Med* 1996; 36: 503-508.
- Amundsen T, Kvaerness J, Jones RA, Waage A, Bjermer L, Nilsen G, Haraldseth O. Pulmonary embolism: detection with MR perfusion imaging of lung—a feasibility study. *Radiology* 1997; 203:181-185
- Berthezene Y, Croisille P, Bertocchi M, Houzard C, Bendib K, Revel D Lung perfusion demonstrated by contrast-enhanced dynamic magnetic resonance imaging. Application to unilateral lung transplantation. *Invest Radiol* 1997; 32:351-356
- Guckel C, Schnabel K, Deimling M, Steinbrich W. Solitary pulmonary nodules: MR evaluation of enhancement patterns with contrast-enhanced dynamic snapshot gradient-echo imaging. *Radiology* 1996; 200:681-686
- Slone RM, Pilgram TK, Gierada DS, et al. Lung volume reduction surgery: comparison of preoperative radiologic features and clinical outcome. *Radiology* 1997; 204:685-693.
- Gierada DS, Slone RM, Bae KT, et al. Pulmonary emphysema: comparison of preoperative quantitative CT and physiologic index values with clinical outcome after lung-volume reduction surgery. *Radiology* 1997;205: 235-242.
- Wang SC, Fischer KC, Slone RM, et al. Perfusion scintigraphy in the evaluation for lung volume reduction surgery: correlation with clinical outcome. *Radiology* 1997; 205:243-248.
- Hatabu H, Tadamura E, Kim D, Li W, Prasad PV, Edelman RR. Pulmonary perfusion: parametric analysis with dynamic contrast-enhanced MRI using ultrashort TE and inversion recovery turbo FLASH. *Proceedings, Society of Magnetic Resonance, Fifth Meeting*. Vancouver, 1997:186.
- Hatabu H, Gaa J, Kim D, Li W, Prasad PV, Edelman RR. Pulmonary perfusion and angiography: evaluation with breath-hold enhanced three-dimensional fast imaging steady-state precession MR imaging with short TR and TE. *AJR* 1996; 167: 653-655.
- Meaney JF, Weg JG, Chenevert TL, Stafford-Johnson D, Hamilton BH, Prince MR. Diagnosis of pulmonary embolism with magnetic resonance angiography. *N Engl J Med* 1997; 336:1422-1427
- Edelman RR, Siewert B, Adamis M, Gaa J, Laub G, and Wielopolski P. Signal targeting with alternating radiofrequency (STAR) sequences: application to MR angiography. *Magn Reson Med* 1994; 31: 233-238.
- Hatabu H, Wielopolski PA, Edelman RR. Pulmonary perfusion MR imaging with ultrashort TR/TE GRE sequence and signal targeting with alternating RF. *Radiology* 1995; 197(P):231.
- Hatabu H, Wielopolski P, Tadamura E. An attempt of pulmonary perfusion imaging utilizing ultrashort TE turbo FLASH sequence with signal targeting and alternating radio-frequency. *Eur J Radiol* 1999; 29:160-163.
- Hatabu H, Tadamura E, Prasad PV, Buxton R, Edelman RR. Noninvasive pulmonary perfusion imaging by STAR-HASTE sequence. *Magn Reson Med* 2000; 44:808-812.
- Paulling L, Coryell C. The magnetic properties and structure of the hemochromogens and related substances. *Proc Natl Acad Sci USA* 1936; 22:159-163
- Young IR, Clarke GJ, Bailes DR, Pennock JM, Doyle FH, Bydder GM. Enhancement of relaxation rate with paramagnetic contrast agents in NMR imaging. *J Comput Tomogr* 1981; 5:543-546.
- Gore JC, Doyle FH, Pennock JM. Relaxation rate enhancement observed in vivo by NMR imaging. In: Partain CL, James AE, Rollo FD, Price RR, eds. *Nuclear magnetic resonance (NMR) imaging*. Philadelphia: WB Saunders, 1983; 94-106.
- Tripathi A, Bydder GM, Hughes JMB, et al. Effect of oxygen tension on NMR spin-lattice relaxation rate of blood in vivo. *Invest Radiol* 1984; 19:174-178.

33. Edelman RR, Hatabu H, Tadamura E, Li W, Prasad PV. Noninvasive assessment of regional ventilation in the human lung using oxygen-enhanced magnetic resonance imaging. *Nature Med* 1996; 2:1236-1239
34. Tadamura E, Hatabu H, Li W, Prasad PV, Edelman RR. Effect of oxygen inhalation on relaxation times in various tissues. *JMRI* 1997; 7:220-225.
35. Albert MS, Cates GD, Driehuys B et al. Biological magnetic resonance imaging using laser-polarized ^{129}Xe . *Nature* 1994; 370:199-201.
36. Middleton H, Black RD, Saam B et al. MR imaging with hyperpolarized ^3He gas. *Magn Reson Med* 1995; 33:271-275.
37. MacFall JR, Charles HC, Black H, et al. Human lung air spaces: potential for MR imaging with hyperpolarized He-3. *Radiology* 1996; 200:553-558.
38. Ebert M, Grossmann T, Heil W, Otten WE, Surkau R, Leduc M, Bachert P, Knopp MV, Schad LR, Thelen M Nuclear magnetic resonance imaging with hyperpolarised helium-3. *Lancet* 1996; 347:1297-1299
39. Kauczor HU, Hofmann D, Kreitner KF, Nilgens H, Surkau R, Heil W, Potthast A, Knopp MV, Otten EW, Thelen M Normal and abnormal pulmonary ventilation: visualization at hyperpolarized He-3 MR imaging. *Radiology* 1996 Nov;201(2):564-8
40. Kauczor HU, Ebert M, Kreitner KF, Nilgens H, Surkau R, Heil W, Hofmann D, Otten EW, Thelen M Imaging of the lungs using ^3He MRI: preliminary clinical experience in 18 patients with and without lung disease. *J Magn Reson Imaging* 1997; 7:538-543
41. Mugler JP 3rd, Driehuys B, Brookeman JR, Cates GD, Berr SS, Bryant RG, Daniel TM, de Lange EE, Downs JH 3rd, Erickson CJ, Happer W, Hinton DP, Kassel NF, Maier T, Phillips CD, Saam BT, Sauer KL, Wagshul ME. MR imaging and spectroscopy using hyperpolarized ^{129}Xe gas: preliminary human results. *Magn Reson Med* 1997; 37:809-815
42. Wagshul ME, Button TM, Li HF, Liang Z, Springer CS, Zhong K, Wishnia A In vivo MR imaging and spectroscopy using hyperpolarized ^{129}Xe . *Magn Reson Med* 1996; 36:183-191
43. Goodson BM, Song Y, Taylor RE, Schepkin VD, Brennan KM, Chingas GC, Budinger TF, Navon G, Pines A In vivo NMR and MRI using injection delivery of laser-polarized xenon. *Proc Natl Acad Sci U S A* 1997; 23;94:14725-14729
44. Albert MS, Balamore D. Development of hyperpolarized noble gas MRI. *Nucl Instr Meth in Phys Res* 1998; A402:441-453.
45. Hatabu H, Chen Q, Levin DL, Tadamura E, Edelman RR. Ventilation-Perfusion MR imaging of the lung. *MRI Clin North Amer* 1999; 7:379-392.
46. Hatabu H. MR Pulmonary angiography and perfusion imaging: recent advances. *Sem US CT MRI* 1997; 18:349-361.

Why and How Should Emphysema Be Quantified on CT?

Alexander A. Bankier, MD

Department of Radiology, University of Vienna, Austria

Learning Objectives

At the end of this lecture, the participants will

1. be aware of the epidemiological and socio-economic importance of pulmonary emphysema;
2. be familiar with the basic technical tools and parameter used and required to accurately quantify emphysema on CT;
3. have learned about the emerging role of functional imaging and the use of advanced techniques in the quantification of pulmonary emphysema on CT.

Why Should Emphysema Be Quantified on CT?

• *Pulmonary emphysema is a very common disease*

Pulmonary emphysema is defined as an “abnormal permanent enlargement of the air spaces distal to the terminal bronchioles, accompanied by destruction of the alveolar walls, and without obvious fibrosis”. In the western world, pulmonary emphysema is among the most common respiratory disorders. Although essentially linked to tobacco smoking, a variety of other agents can contribute to the development of emphysema. Emphysema thereby became a substantial public health problem. As emphasized by G.L. Snider “in many ways, emphysema is to the pneumologist of the last half of the twentieth century what tuberculosis was to the pneumologist in the first half of the twentieth century.” (1)

• *Pulmonary emphysema is a very expensive disease*

Pulmonary emphysema is a chronic disorder. Patients suffer from emphysema for years, sometimes for decades. This creates high costs for care and rehabilitation. Depending on epidemiological factors, these costs may vary. In virtually all countries of the western world, however, emphysema is among the “top five” diseases in terms of morbidity associated health care costs.

• *We know relatively little about the in-vivo natural history of emphysema in humans*

Most studies investigating the development of emphysema, notably in the early stages of disease, have been conducted in animals. Also, many long-term studies are based on animal experiments. It therefore

remains unknown whether data obtained from those studies will remain valid in the context of human emphysema. This issue urges for a technology that allows to detect and follow human emphysema in-vivo. CT fulfills most of requirements that such a technology should have. This substantially stimulated the interest of researchers in CT as a modality used for the longitudinal follow-up of patients with emphysema (2).

• *Promising techniques and interventions for the treatment of emphysema did recently arise*

Lung Volume reduction Surgery (LVRS) is a therapeutic option for patients with severe debilitating emphysema. LVRS consists of bilateral wedge resection of emphysematous lung by means of sternotomy, bilateral thoracotomy, or video-assisted thoracoscopic surgery. LVRS appears to improve lung function, exercise tolerance, and quality of life improvement, peaking at 3-6 months after surgery and maintained for about 2 years. The retrospective nature of patient selection and the inability to accurately quantify the amount of resected emphysematous lung tissue are two major obstacles to define the criteria for selecting LVRS candidates. Patients are usually selected on the basis of clinical, physiological, and plain radiographic criteria. Intolerable dyspnea and exercise intolerance not palliated by therapy, and severe airflow obstruction are clinical key criteria. On the other hand, anatomic features such as the lobar severity of emphysema, with a heterogeneous distribution of emphysema, do contribute to determine the clinical outcome. Upper lobe predominance, a high amount of regional heterogeneity, and a larger percentage of normal or mildly emphysematous lung show the strongest correlation with improvement of the quality of life and exercise tolerance. In this context, several studies have analyzed the relation between preoperative CT findings and postoperative results. Giereda et al. showed that the values of quantitative CT indexes of global and regional emphysema severity were related to outcome measures after LVRS (3). Kazerooni et al. found that a high upper/lower lung emphysema ratio was the best predictor of improvement in term of functional tests and 6-minute walking distance until two years after bilateral apical LVRS (4). Both studies thus indicate that CT

quantification of emphysema could play an important role in identifying the most suitable candidates for LVRS and in standardizing the preoperative evaluation of these patients.

It was long thought that, once damaged, alveoli could not be repaired in the adult lung. Recent studies, however, found that interventions focussing the cellular and biochemical process of alveolar destruction could eventually stop alveolar destruction and even partly restore or replace the destroyed alveolar tissue or volume (5). Although all current knowledge is based on animal studies, the therapy of emphysema would very likely be revolutionized if the results prove to be equally valid in humans. This would require intensive in-vivo monitoring of the drugs in question, and CT might therefore be the technique of choice.

How Should Emphysema Be Quantified on CT?

• *Subjective or objective quantification?*

Subjective scoring systems of emphysema are easy to apply and do not require a highly developed technical environment. The main advantage of computer assisted objective quantification is the reproducibility of the technique across readers of varying experience and expertise, and institutions, that allow more accurate comparisons of results among different medical centers. In a series of 62 patients who underwent thin section CT prior to surgical lung resection, Bankier et al. (6) compared both objective CT quantification and subjective scoring to a macroscopic reference method. Based on visual scoring by three readers of varying experience in two reading sessions, the authors found that subjective scoring was less correlated to both the macroscopic reference and to objective quantification by CT densitometry. Subjective grading also suffered from a systematic overestimation of emphysema. Moreover, subjective grading was compromised by only moderate interobserver agreement. It also was noticeable that the strongest correlation between subjective scoring and macroscopy was achieved by the least experienced reader. This reader also showed the weakest inter-reader agreement. This study suggests that subjective visual grading should be supplemented with more reliable objective methods whenever a precise and reader-independent quantification of emphysema is required.

• *CT scanning in inspiration or expiration?*

Based on comparisons between objective CT quantification and pulmonary function tests, early studies have suggested a potential role for expiratory CT in the quantification of emphysema. Using a similar

technique, more recent studies found a substantial difference between the accurate density thresholds used to quantify emphysema in inspiration and in expiration. It also was shown that expiratory CT underestimates the degree of emphysema as compared to inspiratory CT. It therefore appears that expiratory CT is not as accurate as inspiratory CT for the quantification of emphysema. Data derived from expiratory CT, however, do more accurately reflect functional airflow obstruction than data derived from inspiratory CT.

• *“Thin” or “thick” CT sections?*

Early CT studies of pulmonary emphysema were based on thick (10mm) sections. Since the introduction of thin section CT, however, most CT research has been conducted using thin (1-2mm) slices. There is, indeed, a rationale for the use of thin sections. Other than thick section CT, thin section CT often allows a morphologic differentiation between centrilobular and panlobular emphysema. Thin section CT is also more accurate in demonstrating the morphology of emphysematous destruction with respect to the secondary pulmonary lobule. Virtually all recent validations with macroscopic and microscopic techniques have been performed using thin section CT. Moreover, the density thresholds currently used have been validated on the basis of thin section CT. These points thus favor the use of thin CT sections for the quantification of emphysema.

• *Which density threshold to choose?*

CT scanning provides transverse anatomical pictures in which the value of each picture element (i.e., pixel) is related to the X-ray attenuation of a defined volume of tissue (i.e., voxel). The x-ray attenuation is related to tissue density and is numerically expressed in Hounsfield units (HU). The scale of attenuation values ranges between -1024 HU to 3078 HU, zero corresponding to the attenuation value of water. Hayhurst et al., in the first pathologic-CT comparative study, showed that the distribution curve of attenuation values was significantly shifted toward lowest attenuation values in patients with emphysema compared to normal individuals (7).

In a CT-pathologic correlation study considering microscopic measurements, Gould et al. (8) used the lowest fifth percentile of the histogram of attenuation values. The lowest fifth percentile depends on the extent of emphysema but is also influenced by the relative amount of higher attenuation values, corresponding to airway walls, blood vessels, and any infiltrate, which tends to displace the histogram to the right. To overcome this limitation, an absolute threshold

should be used and the relative area of lung occupied by attenuation values lower than this threshold should be considered. In 1988, Müller et al. (9) used a CT program called “Density Mask” that highlights voxels within a given density range and that automatically gives the area of highlighted voxels. In their study, Müller et al. compared the relative area highlighted on a single 1-cm thick CT slice after injection of contrast material with the corresponding macroscopic section of the fixed lung cut in the same plane as the CT scan and graded using a modification of the picture-grading system of Thurlbeck et al.. The highest correlation was observed by highlighting voxels with attenuation lower than -910 HU. Significant correlations, however, do only indicate that CT and pathological scores are statistically linked, but they do not imply that the percentage area obtained by CT quantifications are equal to those obtained from pathological assessment. Furthermore, the grading panel is a ranking method and does not represent the extent of lung involved by emphysema. Finally, the threshold proposed in the study of Müller et al. could in part have resulted from the injection of contrast material.

Gevenois et al. (10, 11) used a program that automatically recognizes the lungs, traces the lung contours, determines histograms of attenuation values, and calculates the lung area occupied by pixels included in the predetermined range of attenuation value. In this study, the relative areas of lung occupied by attenuation values lower than various thresholds were calculated. The 1-mm collimation scans were performed without injection of contrast material from the lung apices to the bases, with 1-cm intervals. Indeed, emphysema has a heterogeneous distribution throughout the lung, and no study has defined the minimum number of scans necessary to provide accurate results. On a first study using this method based on 63 patients, Gevenois et al. demonstrated, by comparison with pathologic measurements on horizontal paper-mounted lung sections, that the measure of the relative area of lung occupied by attenuation values lower than -950 HU (RA_{950}), calculated on thin section CT obtained at full inspiration, appears to be a method allowing an objective quantification of macroscopic emphysema in-vivo and with an acceptable error. In the same study, they failed to recommend a maximal interval distance between the CT slices valuable for every subject. In a later study, Mishima et al. considered the influence of different thin section CT scanning parameters on the percent ratio of low attenuation area to whole lung field. They compared the low attenuation area obtained with various number of slices ranging from 3 to 10, various slice thicknesses from 2 to 5-mm, and vari-

ous electric tube currents ranging from 50 to 250 mA. On the basis of correlations with lung function, they suggested that three 2-mm thick CT sections, acquired with 250 mA are the most appropriate CT method in order to the follow-up of emphysema (12).

Mc Lean et al. recommended to measure emphysema microscopically rather than macroscopically. Subsequently, Gould et al. compared the lowest fifth percentile of the frequency distribution curve of attenuation values with the distal airspace surface area measured by a microscopic image analysis system (8). They showed that CT scan was able to quantify mild to moderate emphysema. In a more recent study based on 56 patients, Gevenois et al. measured mean diameter and perimeter of alveoli and alveolar ducts (10). They compared the percentage surface area of lung occupied by attenuation values lower than various thresholds to microscopic measurements and they showed that the highest correlation corresponded to -950HU. Both, the earlier macroscopic study and the microscopic study performed by Gevenois et al. suggested thus strongly that RA_{950} is a valuable threshold to quantify pulmonary emphysema. By calculating the upper 95% limit of predicted normal values on a small number of subjects without emphysema, they also suggested that the normal upper limit for RA_{950} is ~7%. Nevertheless, the normal value of RA_{950} could be influenced by various parameters. Indeed, in another study, Gevenois et al. also showed that RA_{950} is influenced by the lung size assessed by the total lung capacity and, to a lesser degree, by age but not by sex.

Several studies suggested that possible errors secondary to variability of lung volume at which CT scans are obtained could be avoided by using a spirometric control triggering the CT acquisition according to a predetermined lung volume. In these studies, the reproducibility, however, was assessed over a short period of time. A recent study showed that spirometric control during scanning is not successful in keeping the inspiration level constant over the years (13). The precision of the delineation of lung contours may also influence the reproducibility of CT lung parameters. In early studies, outlining of the lung contours was made manually but more recently, rapid as well as reproducible automated methods were available on commercially available CT units.

• *Further problems to be solved*

According to current knowledge, CT plays an important role in the quantification of pulmonary emphysema. Nevertheless, this technique is not yet standardized and important questions are still unsolved. Further work is required to establish universal values of reference; to investigate the long-term temporal re-

producibility of CT measurements; to compare CT techniques respectively based on a lowest percentile histogram frequency distribution curve and on absolute thresholding; to evaluate the accuracy of CT, not only in the quantification but also in the characterization of pulmonary emphysema; to further investigate the influence of technical CT parameters on the quantification of the disease; to validate new CT techniques such as multidetector systems; to investigate the ability of CT to reliably discriminate pulmonary emphysema from other chronic obstructive respiratory disorders; to determine the capability of CT to characterize the subtypes of pulmonary emphysema.

REFERENCES

1. Snider GL, Kleinerman JL, Thurlbeck WM, Bengali ZH. The definition of emphysema. Report of a national Heart, Lung, and Blood Institute, Division of Lung Disease Workshop. *Am Rev Respir Dis* 1985;132: 182-185.
2. Gevenois PA, Yernault JC. Can computed tomography quantify pulmonary emphysema ? *Eur Respir J*. 1995 ; 5 :843-848.
3. Gierada DS, Slone RM, Bae KT, Yusen RD, Lefrak SS, Cooper JD. Pulmonary emphysema: comparison of preoperative quantitative CT and physiologic index values with clinical outcome after lung volume reduction surgery. *Radiology* 1997; 205: 235-242.
4. Kazerooni EA. Radiologic evaluation of emphysema for lung volume reduction surgery. *Clinics in chest medicine*1999; 20: 45-86.
5. Belloni PN, Garvin L, Mao CP, Bailey-Healy I, Leaffer D. Effects of all-*Trans*-Retinoic Acid in promoting alveolar repair. *Chest* 2000; 117: 235S-241S.
6. Bankier AA, de Maertelaer V, Keyzer C, Gevenois PA. CT of pulmonary emphysema: subjective assessment and objective quantification by densitometry and macroscopic morphometry. *Radiology* 1999; 211: 851-858.
7. Hayhurst MD, Flenley DC, McLean A, Wightman AJA, MacNee W, Wright D, Lamb D, Best J. Diagnosis of pulmonary emphysema by computerised tomography. *Lancet* 1984; 2: 320-322.
8. Gould GA, Macnee W, McLean A, Warren M, Redpath A, Best JJK, Lamb D, Flenley DC. CT measurements of lung density in life can quantitate distal airspace enlargement: an essential defining feature of human emphysema. *Am Rev Respir Dis* 1988; 137: 380-392.
9. Müller NL, Stapels CA, Miller RR, Abboud RJ. "Density Mask": an objective method to quantitate emphysema using computed tomography. *Chest* 1988; 94: 782-787.
10. Gevenois PA, De Vuyst P, de Maertelaer V, Zanen J, Jacobovitz D, Cosio MG, Yernault J-C. Comparison of computed density and microscopic morphometry in pulmonary emphysema. *Am J Respir Crit Care Med* 1996; 154: 187-192.
11. Gevenois PA, de Maertelaer V, De Vuyst P, Zanen J, Yernault JC. Comparison of computed density and macroscopic morphometry in pulmonary emphysema. *Am J Respir Crit Care Med* 1995; 152: 653-657.
12. Mishima M, Hirai T, Itoh H, Nakano Y, Sakai H, Muro S, Nishimura K, Oku Y, Chin K, Ohi M, Nakamura T, Bates J, Alencar AM, Suki B. Complexity of terminal airspace geometry assessed by lung computed tomography in normal subjects and patients with chronic obstructive pulmonary disease. *Proc Natl Acad Sci* 1999; 96: 8829-8834.
13. Stoel BC, Vrooman HA, Stolk J, Reiber JHC. Sources of error in lung densitometry with CT. *Invest Radiol* 1999; 34: 303-309.

The Role of MRI in Ischemic Heart Disease

Jack A. Ziffer, MD, PhD

At the time of publication, no abstract was available.

Disclosure Statement: Speakers Bureau, DuPont, Fugisawa.

Helical CT and Electron-Beam CT Imaging of Coronary Calcium: An Update

William Stanford, MD

Professor, Chest and Cardiovascular Imaging

Department of Radiology

University of Iowa College of Medicine

Objectives

1. To understand the pathophysiology of coronary artery atherosclerotic plaque development.
2. To understand the new advances in imaging of coronary calcification.
3. To be updated on the current information relative to use of Electron Beam and Helical CT scanning of coronary artery calcification.

Coronary Atherosclerosis-Pathophysiology

Calcification within the wall of a coronary artery is a recognized marker of atherosclerosis. Computed tomography (CT), and especially the faster Electron Beam CT (EBT) and helical-CT (HCT), are especially sensitive in detecting coronary artery calcification. Thus, these imaging modalities are becoming increasingly important in detecting preclinical coronary artery disease.

The development of coronary atherosclerosis is thought to occur secondary to an injury of the coronary endothelium. This injury allows circulating histiocytes to traverse the injured endothelium and lodge in the arterial wall there they are transformed into macrophages. As macrophages, these cells can accumulate lipid and, by an active metabolic process, promote calcification and the proliferation of smooth muscle cells. This early deposition of lipid can be seen as “fatty streaks” beneath the surface endothelium of the coronary vessel. As the lipid accumulates, it may distort the vessel wall without encroaching on the arterial lumen; this process is called remodeling. In these instances, the coronary arteriogram may be entirely normal.

The lipid accumulation is usually covered by a thin fibrous cap. If the cap ruptures, and allows circulating blood to come in contact with the lipid and smooth muscle cells, an intense thrombogenic reaction can occur. Depending upon the size of the artery, location of the plaque, and extent of collateral circulation, several events can happen. There could be a

complete occlusion of the coronary artery with sudden myocardial infarction and death or an infarction with survival but with residual myocardial damage. Conversely, if collateralization is adequate, there may be minimal to no residual damage after the occlusion. However, with repeated episodes, the lumen frequently narrows, and fixed stenoses develop.

Calcium Deposition and Plaque Rupture

Calcium hydroxyapatite is thought to precipitate in diseased coronary arteries via a mechanism similar to that found in active bone formation and remodeling. Although there may be several mechanisms involved in calcium deposition, a close relationship appears to exist between cholesterol and calcium deposition. In fact there appears to be a correlation between EBCT calcium and the total atherosclerotic plaque burden. Rumberger et al have reported that the volume of calcified plaque was approximately 1/5 of that of associated noncalcified plaque. Hence, these data suggest that calcified plaque can act as an indicator for the presence of soft, relatively unstable plaque.

CT Imaging of Coronary Atherosclerosis

IMAGING MODALITIES

Electron-Beam CT

The majority of published literature has targeted the EBT detection of coronary artery calcium using 100 millisecond, 3 millimeter contiguous images and with this technology calcified plaques are readily seen. Scoring is by placing regions of interest manually around the plaques to measure the threshold of pixels present in each individual plaque.

Calcifications are reported as the volume score or the Agatston score. The Agatston score arbitrarily assigns values dependent upon the amount of calcification present in the lesion. The sum of the Agatston scores would represent the total calcifications within a single artery or, if the score of all the arteries were summed, the total calcium score would be reported.

Helical CT

Helical CT scoring is done in a similar way, however, some investigators have suggested that a Helical CT threshold of +90 HU gives better accuracy in calculating the calcium score than a threshold of +130 HU. Since few other studies have supported these thresholds and since EBT values of +130 HU are the standards most commonly reported in the literature, a +130 HU value is the most frequently utilized in reporting coronary calcium scores for both EBT and HCT.

Calcium as a Predictor of Atherosclerotic Disease and Stenosis

In 1990, Agatston et al reported the first large clinical series in which EBT was used to detect calcification of the coronary arteries. A total of 584 consecutive patients (mean age, 48 years) underwent 3-mm, 100msec EBT scans; 50 also underwent fluoroscopic examinations. One hundred nine patients had coronary artery disease established by a history of myocardial infarction (22 patients) or angiographic evidence of more than 50% diameter narrowing on coronary angiography (87 patients). The remaining 475 patients had no history of coronary disease. Patients with a history of coronary artery disease consistently had more calcium than comparably aged individuals with no history of coronary artery disease ($p < 0.0001$). In this study a total calcium score of 300 had sensitivity of 74% and a specificity of 81% for indicating obstructive disease. The negative predictive value of a zero calcification score was 98%.

A larger multicenter study that examined coronary calcification as an indicator of significant stenosis involved 710 patients presenting with symptoms of coronary artery disease. There were 456 men and 254 women (mean age, 56 years). In this group, the sensitivity of EBCT in detecting calcification as an indicator of significant stenosis (>50% narrowing) was 95%, and the specificity was 44%. The positive predictive value was 72%, and the negative predictive value was 84%.

Although EBT is extremely sensitive in defining coronary vascular calcification, the extent and location of the calcification does not necessarily equate with site-specific stenosis. Stanford et al examined data from 150 patients undergoing EBT scans and coronary arteriography and found only one patient with greater than 50% narrowing in the absence of calcification. Thus, the absence of calcification appears to negate the presence of significant stenosis.

Gender differences also play a role in the development of coronary calcification. In a study evaluating

the prevalence of coronary calcification at intervals of 5-10 years in 1,396 male and 502 female asymptomatic subjects (age range, 14-88 years), Janowitz et al found that the prevalence of coronary calcium in women was half that of men until age 60 years when the difference diminished. The calcium distributions in men aged 40-69 years were virtually identical to those in women aged 50-79 years.

Progression of calcified plaque was also evaluated in a study by Janowitz et al. These investigators evaluated calcific plaque in 25 symptomatic and asymptomatic individuals 406 days (mean) apart. Patients with proven obstructive coronary artery disease by angiography had a 48% increase in the calcium scores as compared with a 22% increase in asymptomatic subjects. Patients with obstructive coronary artery disease also had 55 new calcific deposits on the follow up study versus 18 in the asymptomatic group.

Coronary Calcium as a Predictor of Cardiac Events

Although the presence or absence of calcification appears related to overall atherosclerotic plaque burden, it is event data that are important in establishing the true clinical significance of coronary artery calcification.

A multicenter EBT calcium study reviewed event data in 501 patients undergoing both an EBT calcium study and coronary angiography. Most of these individuals had presented with symptomatic coronary artery disease. In this group, 1.8% died and 1.2% had nonfatal myocardial infarctions during a mean follow-up period of 31 months. A calcium score of 100 or greater was shown to be highly predictive in separating patients with cardiac events from those without events. In this study, logistic regression, which included calcium score, age, gender, and coronary angiographic findings as independent variables, showed that only the log calcium score predicted events.

A recent study at Arad et al has also shown a strong correlation between coronary calcification and the prediction of cardiac events in an asymptomatic group of individuals undergoing catheterization for other than suspected coronary artery disease. In this study, 1,136 asymptomatic subjects were followed for 3.6 years (mean). In that time period, there were 40 cardiovascular events including two deaths, 14 myocardial infarctions, 14 coronary bypass operations and 10 coronary angioplasties. For a coronary artery calcium score of 600 (representing 50% stenosis), the sensitivity was 80%, and the specificity was 85% for predicting cardiac events and the odds for a coronary event were 23 times greater ($p = 0.0001$). From this study Arad et al concluded that EBT had

the potential to predict future cardiovascular events in asymptomatic subjects. Other risk factors, such as the presence of hypercholesterolemia, low high-density lipoproteins, hypertension, diabetes, and family history, failed to predict subsequent events. Conventional risk factors have odds ratios of 4.5 (age), 5.8 (diabetes), 3.7 (hypercholesterol), and 3.0 (hypertension) in predicting cardiac events.

Imaging of Soft (Noncalcified) Plaque

The speed and resolution of the CT scanners are also allowing the identification and possible tissue characterization of soft plaque. These applications are showing great promise in the evaluation of coronary artery disease.

Conclusions

CT has many applications in defining coronary atherosclerosis and assessing ischemic heart disease. Thus CT imaging can provide information for screening patients with coronary artery disease and has an application in evaluating functional aspects in individuals who have sustained cardiac events.

REFERENCES

1. Stanford W, Thompson BH, Weiss RM. Coronary artery calcification: clinical significance and current methods of detection. *Am J Roentgen* 1993; 161:1139-46.
2. Stanford W. Coronary artery calcification as an indicator of preclinical coronary artery disease. *Radiographics* 1999; 19:1401-1419.

Disclosure Statement: W.S. is a member of Toshiba, CT Advisory Board.

Potential Role of MRI in Ischemic Heart Disease

Charles B. Higgins, MD

The major cardiovascular disease encountered in North America is ischemic heart disease. Magnetic resonance imaging (MRI) has not been used extensively for the evaluation of ischemic heart disease because other imaging modalities are entrenched in the informal diagnostic algorithms employed by clinicians. The typical approach is to use echocardiography for ventricular function, nuclear perfusion imaging for myocardial perfusion, and selective angiography for coronary morphology. It is now evident that magnetic resonance imaging (MRI) can provide evaluation of regional ventricular function, myocardial perfusion, and myocardial blood flow (1). Some studies have also shown the feasibility of MR angiography for visualization of the major coronary arteries.

Ventricular Function

MR imaging has been used effectively for the quantification of global and regional left ventricular function. This has been done using cine MR imaging, and more recently, using the breath-hold version of cine MR imaging.

Several studies have demonstrated the correlation between the site of left ventricular dysfunction as demonstrated by MR imaging and the site of acute myocardial infarction. At the site of prior myocardial infarctions, the extent of systolic wall thickening has generally been shown to be less than 2 mm.

The identification of ischemic myocardial dysfunction during pharmacologic stress has been used as a method for demonstrating the presence of ischemic heart disease. Provocative pharmacologic maneuvers have included the use of dipyridamole and dobutamine. In most patients, cine MR imaging performed in the basal state did not demonstrate any regional contraction abnormality. However, performance of the cine MR imaging after the administration of dipyridamole elicited a regional contraction abnormality in most patients. In several studies, stress cine MR imaging has demonstrated a diagnostic accuracy for the detection of regional myocardial ischemic dysfunction equivalent to the diagnostic accuracy of the stress radionuclide perfusion studies.

Stress echocardiography has been used substantially in recent years for the identification of ischemic myocardial dysfunction. Moreover, the assessment of regional myocardial perfusion during exercise and in response to coronary vasodilators using radionuclide

imaging has proven to be reasonably reliable and such studies are easily conducted. It remains to be determined if cine MR imaging during stress will be competitive with these other techniques for the purpose of demonstrating regional myocardial ischemia. In the environment of the MR imager, the performance of stress studies is somewhat more complicated and these studies may prove to be more expensive.

Myocardial Perfusion

Regional myocardial perfusion can be evaluated using the fast cine MR imaging techniques after the intravenous injection of MR contrast media. For the monitoring of the first pass of MR contrast media, fast cine MR imaging techniques are utilized using inversion recovery prepared fast gradient echo imaging or inversion recovery echoplanar imaging. T1-enhancing contrast media produced enhancement of normally perfused myocardium but did not enhance the region during the first pass of the contrast media. Consequently, the ischemic region is demonstrated as a region of low signal intensity (cold spot).

In an animal model of critical coronary stenosis produced by controlled stenosis of the circumflex coronary artery, inversion recovery prepared fast gradient echo imaging was used to monitor the first pass of T1-enhancing contrast media (2). In these animals, Doppler flow meters on the left anterior descending and circumflex coronary arteries continuously monitored coronary blood flow, and the severity of the stenosis was regulated so that reactive hyperemia was completely ablated. This produced only a slight decrease in coronary blood flow in the basal state, but ablated the increase in blood flow in response to dipyridamole. The fast cine MR imaging after contrast media demonstrated equivalent enhancement of all regions of the myocardium in the basal state. However, in response to dipyridamole, which increased flow in the normal coronary artery by several fold, there was markedly decreased and delayed enhancement of the ischemic region compared to normal myocardium on fast gradient echo imaging.

In patients, regional myocardial perfusion has been assessed using fast GRE imaging techniques after the administration of MR contrast media. In these studies, the peak enhancement and rate of rise of signal intensity in the ischemic region was less

than that of normal myocardium. A study in our laboratory (3) combined the assessment of regional myocardial function using breath-hold cine MR imaging and first pass monitoring of the distribution of contrast media using inversion recovery prepared fast gradient echo imaging in patients with perfusion abnormality as demonstrated by radionuclide perfusion imaging. In this study, approximately 90% correlation was demonstrated between the radionuclide perfusion study and the cine MR perfusion and/or regional function abnormalities.

Coronary Anatomy

Manning, Edelman, and co-workers (4) have demonstrated encouraging results with the use of modified versions of breath-hold cine MR imaging for demonstrating the anatomy of the coronary circulation in man. These investigators have shown high accuracy between cine MR angiographic techniques and X-ray coronary angiography for demonstrating hemodynamically significant coronary arterial stenoses. Another report (5) has shown less success of coronary MRA for detecting coronary arterial stenoses and has pointed out some pitfalls for the MRA technique. However, it is clear that with sufficient experience, relatively long segments of the major coronary arteries can be demonstrated using breath-hold cine MR imaging techniques (6).

Coronary Blood Flow

Perhaps the most exciting possibility with cine MR imaging techniques is the quantification of myocardial blood flow and blood flow velocity. It is now

realistic to assume that if one can visualize the coronary arteries on breath-hold cine MR images, then it is possible to measure blood flow velocity in these vessels. Using breath-hold velocity encoded cine MR imaging, the blood flow velocity has been monitored during the cardiac cycle. Moreover, using these techniques, it has been possible to assess vasodilator reserve in the left anterior descending coronary artery in response to dipyridamole and adenosine (7).

Cine MR imaging techniques can also be used for demonstrating the patency of coronary artery bypass grafts. Moreover, flow and flow reserve in grafts can be assessed using velocity encoded cine MR imaging before and after the administration of vasodilators.

REFERENCES

1. Steffens JC, Sakuma H, Bourne MW, Higgins CB. MR imaging in ischemic heart disease. *Am Hrt J*, 1996 July; 156-173.
2. Saeed M, Wendland MF, Sakuma H, Higgins CB. Coronary artery stenosis: detection with contrast enhanced MR imaging in dogs. *Radiology*, 1995; 196:79-84.
3. Higgins CB, Saeed M, Wendland MF, Bourne M, Steffens JC, Sakuma H. Evaluation of myocardial function and perfusion in ischemic heart disease. *N Engl J Med*, 1993; 328:3823-3832.
4. Duerinckx A, Urman MK. Two-dimensional coronary MRA: analysis of initial clinical results. *Radiology*, 1994; 193:731-738.
5. Pennel DJ, et al. Assessment of coronary artery stenosis by MRI. *Heart*, 1996.
6. Sakuma H, Blake LM, Amidon TM, O'Sullivan M, Higgins CB, et al. Coronary flow reserve: measurement in humans with breath-hold velocity encoded cine MR imaging. *Radiology*, 1996; 198:745-750.

Cardiac Imaging with Multidetector-Row CT

Geoffrey D. Rubin, MD

The introduction of multidetector row CT has rejuvenated interest in CT applications for cardiac imaging. This is due to several unique technical features of multidetector-row MDCT scanners, which will be described in this, abstract. Following a description of these technical features, an overview of clinical applications for multidetector row CT in the heart will be presented.

Technical Considerations

Although the advantages of multidetector row CT for acquiring large extra-cardiac vascular data sets are well recognized, the enhanced speed of acquisition, which is attributable to the use of high table feed rates coupled with narrow section thickness, does not specifically offer any advantages toward diminishing the motion of the heart. It is the combination of cardiac contraction, rotation, and translation that occurs with every heartbeat that has traditionally degraded the quality of cardiac CT. For CT to play an important role in the assessment of the heart, the temporal resolution must substantially improve over traditional values which prior to MDCT have corresponded to the gantry rotation period of one second or longer. Although shorter gantry rotation periods can serve to diminish cardiac motion as has been demonstrated by the electron beam CT scanner which has a beam sweep time as low as 50 milliseconds, traditional MDCT scanners which like traditional CT scanners rely on mechanically rotating gantries have not achieved rotation times less than 0.5 seconds.

The reduction of the temporal resolution of MDCT scans beyond that of the gantry rotation period begins with the use of a half scan interpolation algorithm. This algorithm, which has been called 'segmented reconstruction' by several CT scan manufacturers, uses 180 degrees plus the x-ray fan angle of approximately 40-45 degrees for a total of approximately 225 degrees of data to reconstruct a transverse section. Although this reconstruction approach is associated with image artifacts that present as low attenuation shading across the image particularly in regions of high attenuation differences. It can reduce the temporal resolution of a one second gantry rotation period CT scanner to 0.6 seconds and a 0.5 second gantry rotation period to 0.3 seconds.

This technique has been used in single-detector

row CT (SDCT) scanners for the purpose of imaging coronary calcium. Note however that this temporal resolution is three times slower than the fastest 512 x 512 acquisition of the EBCT scanner (100 ms).

Nevertheless, this reconstruction strategy forms the basis of "prospective" cardiac gating techniques. Prospective gating is performed when an ECG waveform is available to trigger the CT acquisition during some phase of the cardiac cycle, typically diastole. This method requires a "step-and-shoot" mode typical of conventional CT scanning. With a four detector row CT scanner, four sections are acquired during diastole of the first heart beat. The table then advances rapidly to acquire the second set of four images either during the next heartbeat or after skipping a beat depending upon the heart rate and the minimum interscan delay time allowed by the CT scanner. This technique is currently employed on commercially available software packages for performing coronary calcium screening with either MDCT or SDCT.

There are two primary limitations to performing prospective triggering. One of these limitations is that the acquired data are not helical and therefore do not have the advantages of a helical CT data set such as capability for overlapping reconstruction or continuous data acquisition. The other limitation is that data are only acquired during a single phase of the cardiac cycle. This imposes substantial constraints for assessing coronary anatomy of cardiac function.

The alternative to prospective gating is "retrospective" gating of a helical acquisition. When performing retrospective gating, the ECG tracing is recorded simultaneous with the helical acquisition. Sections are retrospectively reconstructed at specific time increments within the cardiac cycle to provide a volumetric data set of the heart that corresponds to a single time frame within the cardiac cycle. When using simple half-scan interpolation with a 0.5 second gantry rotation to reconstruct the data, a 300 millisecond window of time is retrospectively selected relative to the ECG tracing for each heart beat. There is, however, one additional strategy that can be employed to substantially reduce the temporal resolution of the CT scan further. This has been called "multisector" or "multiphasic" reconstruction. The basic principle of multisector or multiphasic reconstruction is that the entire 240 degrees of data required for half-scan

interpolation are not acquired with a single gantry rotation. Rather, a fraction of the required 240 degrees is acquired during successive heartbeats. For example, a two-sector reconstruction strategy would acquire 120 degrees of information during beat one and the complementary 120 degrees during beat two. As a result, the temporal resolution of the scan is reduced in half from 0.3 to 0.15 seconds. Further, a three sector reconstruction could be performed using three successive heartbeats where approximately 80 degrees of data are acquired resulting in a temporal resolution of 100 milliseconds. Note that this strategy is only possible with a MDCT scanner, as it mandates that after the first sector is acquired with the leading row of detectors, there are additional detectors in line to image the successive sectors over the same position of the heart.

Although the temporal resolution of multisector reconstruction is theoretically very impressive, there are two main limitations to this reconstruction strategy. The first is based upon the assumption that the cardiac cycle is identical during successive beats. While this is clearly not the case for patients with arrhythmia, it is unlikely to be the case in patients with normal sinus rhythm simply due to typical beat-to-beat variability. As a result, the two or three sectors used to reconstruct a transverse section may be slightly misregistered within the cardiac cycle resulting in some degree of blurring or artifacts.

The second limitation of this approach is that very low pitch values must be used in order to ensure that all sectors can be acquired over the same region of anatomy to reconstruct a transverse section. What should hopefully be evident is that a three sector reconstruction with its 100 millisecond temporal resolution requires a slower table feed than does a two sector reconstruction or a full half scan, which have lesser temporal resolution. The limitations of this lower pitch include a lower table speed which substantially limits patient coverage and a substantial increase in the radiation exposure due to the fact that the same region of the anatomy is exposed during two to three heart beats. While the specific radiation exposure remains less than that of a typical fluoroscopically based contrast enhanced cardiac examination with cine filming, it is substantially higher than standard CT scan dosages.

In spite of these potential limitations, the use of a helical acquisition coupled with MDCT and retrospective gating shows substantial promise for clinical cardiac imaging. Prior to realizing many of these clinical advantages, a number of technical issues need further resolution. These include the optimization of the implementation of the reconstruction algorithms, a thorough understanding of the tradeoffs of using

higher or lower numbers of sectors to reconstruct the data, and the design of CT scanners allow for sufficient variations in gantry rotation period as well as increasing numbers of simultaneous detector row channels to allow coverage of the entirety of the heart with diagnostic image quality independent of the heart rate.

Coronary Calcium

Currently the only routine clinical application for MDCT scanning of the heart is the detection of coronary calcium. Substantial data have been collected regarding coronary calcium scores in both symptomatic and asymptomatic individuals using electron beam CT (EBCT) scanning. Preliminary investigations suggest that there is no significant difference between coronary calcium scores obtained using MDCT scanners when compared to EBCT. These data suggest that the results gleaned from EBCT studies of coronary calcium can be applied to MDCT scanning; however, further data are required to confirm this. Currently the application of perspective triggering is the only means used to score coronary calcium; however, as was previously stated this technique results in substantially lower temporal resolution than EBCT. This property is countered by improved spatial resolution both in the transverse and longitudinal directions when compared to EBCT. Available data comparing MDCT and EBCT have been generated using prospective triggering exclusively.

Preliminary analyses of retrospective triggering suggest that the use of a multisector reconstruction can substantially improve coronary calcium visualization when compared to half-scan reconstruction used for prospective gating. Because retrospective gating is employed with a continuous helical acquisition and the multi-sector reconstruction requires a low scan pitch, the radiation exposure associated with retrospective is gating approximately six times higher than that of prospective gating. Therefore, with the current implementation, retrospective gating is impractical as a means of screening the coronary arteries for calcification.

There are two clinical scenarios that may prove useful for the application of coronary calcium scanning. A detailed discussion of these applications is beyond the scope of this presentation. In short, the most commonly employed application is the assessment of patients between the ages of 40 and 70 years without documented coronary artery disease but some degree of risk for the development of coronary artery disease as determined by standard clinical indices. In this setting, coronary calcium screening has been used as a means of risk stratification with the outcome being that high-risk individuals would be

treated more aggressively with lipid-lowering drugs and encouraged to aggressively pursue lifestyle modification. The second and more controversial application is the assessment of patients with acute chest presenting to the emergency room without definitive evidence for acute myocardial infarction by ECG tracing or serum troponin levels. There are preliminary data that suggest that the absence of coronary calcium in patients presenting with acute chest pain has a very high negative predictive value for the cause of the chest pain being related to coronary artery disease. The potential value of scanning this patient population is that these patients could be immediately discharged from the hospital eliminating the expensive practice of admitting patients with cryptic causes of acute chest pain in order to perform further diagnostic testing in inpatients upon presentation.

CT Coronary Angiography

Without doubt the greatest enthusiasm for cardiac applications of MDCT centers on exciting preliminary data suggesting that MDCT can be applied to perform direct coronary CT angiography. Compelling visualizations of the coronary arterial tree have been created using 1.25 mm section thickness acquisitions that extend from the base of the heart through the apex and demonstrate both normal and diseased first and second order coronary arterial branches. Further, data have suggested that MDCT provides noninvasive visualization of noncalcified mural atheroma and thrombus allowing the delineation of atherosclerotic disease that was previously only possible using highly invasive intravascular sonography.

It is important that the medical community not be overwhelmed by the enthusiasm of these initial anecdotal reports. Our experience applying MDCT angiography to the coronary arteries in approximately 30 patients suggests that the image quality is substantially dependant upon complex patient-related factors including the heart rate and consistency of the cardiac period, among other characteristics. Investigators with the most encouraging results routinely perform beta blockade to reduce the heart rate thereby allowing for a lengthening of the cardiac period, which allows for a longer diastolic phase, which in turn allows the use of a reconstruction strategy that relies upon less sectors for reconstruction. This ad-

vantage while diminishing the overall temporal resolution diminishes the image degradation relating to beat-to-beat variability.

Because coronary CT angiography requires a helical acquisition and therefore retrospective gating, it has become evident that CT hardware with greater flexibility than is currently available will be necessary to provide images that are consistently diagnostic in quality. The use of variable gantry rotation periods as well as an increase in the simultaneous acquisition of eight or more detector rows of information should substantially improve the reliability of this examination, which at this time should be considered purely investigational.

Other Applications

The use of retrospective gating allows for the entire cardiac volume to be reconstructed at arbitrary positions within the cardiac cycle. As result, a four dimensional recording of the heart can be acquired within a 30 to 40 second time frame. This holds substantial promise for providing data for the analysis of cardiac function. Post processing analytical tools will need to be developed to quantify functional indices from these data sets. It has further been suggested that myocardial perfusion can be assessed as well using a diastolic acquisition of first pass contrast-enhanced phenomenon through the myocardium. Finally, the technical advantages associated with MDCT for imaging the heart allow for an assessment of cardiac masses, congenital anomalies, and other structural changes within the heart with a high degree of clarity.

With further experience, cardiac CT is likely to emerge as an important examination for the assessment of many cardiac abnormalities, which are not completely characterized by echocardiography. While magnetic resonance imaging has a substantially longer history of investigation and far more resources directed toward it for the assessment of cardiac disease, the speed, simplicity, easy access and reduced cost of CT scanning will likely make it a preferred alternative for some assessments in specific patient populations. While magnetic resonance imaging is capable of providing information that is unattainable using CT, it will ultimately be the relevance of this information to therapy and clinical outcome that will drive the relative use of these modalities.

Cardiac Diagnosis: How to Approach the Chest Radiograph

Martin J. Lipton, MD

Objectives

- To describe a logical scheme for visual search of the chest, focused on heart disease
- To demonstrate examples of cardiac findings on chest images
- To explain how these can be analyzed to reach a diagnosis
- To emphasize why radiologists should become competent in cardiac imaging

Introduction

Traditional plain chest radiography provides the earliest opportunity for diagnosing all forms of heart disease. This technique is perhaps the most rapid, cost-effective and safest screening procedure for diagnosing lung disorders, however its role in heart disease has been undervalued. Indeed, the most significant limitation of the chest radiograph as a diagnostic tool is the experience and knowledge of the physician who interprets the examination. Furthermore, advances in digital imaging have made improved diagnosis possible by temporal and energy subtraction as well as with magnification and computer aided diagnostic techniques.

Visual Search

Each radiologist should devise a systematic and consistent approach for examining chest images in order to identify cardiac and vascular abnormalities. The following issues should be incorporated into a visual search to evaluate the following:

1. Technical factors
2. Skeletal abnormalities and “hardware”
3. Situs–position of the gastric air bubble, cardiac apex and aortic knob
4. Heart size, position and shape
5. Great vessels–relative size, shape and position
6. Lung fields and vascularity–compare zones bilaterally
7. Identification of calcifications

Spectrum of Patient Presentations

Patients may present in the radiology department at any phase of their illness. Diagnosis may be required for various reasons, such as screening, evaluating the severity of a known disease, and assessing therapy–medical or post-surgical.

Heart Failure

One of the most valuable aspects of chest radiography is identifying the presence and severity of heart failure. Pulmonary haemodynamics can be elegantly evaluated from the plain chest images; indeed pulmonary edema may be seen before physical signs develop.

Congenital Heart Disease (CHD)

CHD is increasingly seen in the adult population as more successful surgical procedures are performed. Over-circulation must be recognized together with changes in the cardiac chambers and great vessels. Furthermore, radiologists should be comfortable in offering a differential diagnosis and a definitive opinion in this situation.

Cardiac Calcification

Calcification within the cardiac silhouette should be actively sought. What is its location, character and nature? Does it depict the walls of a cardiac chamber, valve, or could it be in a coronary artery or the pericardium? Vessel calcification usually appears like tram tracks as two white parallel lines. Pericardial calcification is usually multilayered and often more obvious in the lateral projection, especially along the diaphragm, where the inferior cardiac border lies. Valve calcium is usually more dense, like a white blob or diamond in appearance.

Lung Abnormalities

The lungs may demonstrate vascular malformations, which often look tubular, and have a broad spectrum; other lesions however must also be considered.

Summary

There is a great deal of information readily available from routine frontal and lateral chest images. An organized and disciplined visual search will be rewarded. Many patients, remember, will not be seen by a cardiologist unless the radiologist suspects the diagnosis and makes this recommendation. Patients are often asymptomatic or have minimal disability. Identifying the various abnormalities of cardiovascular disease from chest radiographs should be an enjoyable exercise. Furthermore, it is becoming more important, because cardiac disease still remains the

commonest cause of morbidity and mortality in the adult population. The dramatic advances in CT and MR will be increasingly applied for diagnostic imaging and managing heart disease in the future. Radiologists are fortunate in being given this enormous clinical, scientific and business opportunity. We must embrace it with enthusiasm and interest. If radiologists fail to become actively involved in this field, they will only be involved in diagnostic cardiac imaging in the future, as patients!

SUGGESTED READING

1. Kory RC, Tsagaris TJ and Bustamante RA. A Primer of Cardiac Catheterization, Published by Charles C. Thomas, Springfield, IL 1965.
2. Braunwald E, Ross J Jr, and Sonnenblick EH. Mechanisms of Contraction of the Normal and Failing Heart. *N Engl J Med* 1967;277:794-800/853-862/910-920/962-971/1012-1022 (Selected Readings).

3. Braunwald E. Determinants and Assessment of Cardiac Function. *N Engl J Med* 1977;296:86-89.
4. Higgins CB. Essentials of Cardiac Radiology and Imaging. Published by J.B. Lippincott Co., Philadelphia, Pennsylvania, 1991.
5. Lipton MJ and Rumburger JA. The Assessment of Left Ventricular Systolic and Diastolic Function by Ultrafast Computed Tomography. *Am J Card Imaging* 1991; 5(4):318-327.
6. Boxt LM. Cardiac Physiology. NASCI Teach-the-Teachers Symposium on Cardiac Imaging, May 15-19, 1994, Burlingame, CA.
7. Reagan K, Boxt LM and Katz J. Introduction to Coronary Arteriography. *Radiol Clin N America* 1994; 32(3):419-433.
8. Schlant R, Alexander RW, Lipton MJ, Editors. Diagnostic Atlas of the Heart a companion to The Heart, Hurst's Eighth Edition. Health Professions Division of McGraw-Hill Publishers, New York, New York, 1996.
9. Duerinckx AJ and Lipton MJ: Noninvasive Coronary Artery Imaging Using CT and MRI. *AJR* 1998;170:900-902.
10. Lipton MJ, Boxt LM and Hijazi ZM. Role of the Radiologist in Cardiac Diagnostic Imaging. *AJR* 2000;175:1495-1506.

Teaching Cardiac and Great Vessel Anatomy with CT-derived 3D Reconstructions

A. Rozenshtein, MD¹

L. Bost, MD^{1,2}

1. St. Luke's-Roosevelt Hospital Center, New York, NY

2. Beth Israel Medical Center, New York, NY

We perform radiographic imaging to display normal and pathologic anatomy. When interpreting imagery for these purposes, there is an intellectual interplay between expected normality and the instant appearance of organs and tissues under study. That is, our ability to identify and characterize the abnormal is based to a large extent in our ability to recognize the normal. Furthermore, our ability to identify and characterize normality is based upon our expectation of the appearance and anatomic relations of the organs and tissues.

The intuitive understanding of the intimate relationships of organs inside the human body is inherently three-dimensional. Until recently, the best study aid was the dissection lab, where the three-dimensional structures are presented in a three-dimensional manner, as the layers are peeled off one by one. Unchanged since the Renaissance, this lengthy process allows ample time for familiarizing the student with details. This method is expensive and therefore is not generally available outside medical school anatomy courses. In addition, even in the most experienced hands the layers already removed may not necessarily come back together easily for a repeat demonstration, and the postmortem and post-formaline effects alter the organs in a notably non-physiologic fashion.

Outside the dissection room students of anatomy rely on textbooks and atlases, which present the three-dimensional information in a planar pictorial format, supplemented by a descriptive text. The students are, therefore, required to perform complicated mental manipulations, factoring the planar drawings and written text to achieve the three-dimensional imagery essential to understanding anatomy. Having mastered anatomy in medical school to a various degree, the radiology resident studying cross-sectional imaging is faced with a counterintuitive and lengthy process of stacking sequential axial images and mentally reconstructing the already familiar three-dimensional relationships between organs.

It would be highly desirable to shorten the time required to familiarize the junior residents with normal and abnormal anatomy, and to be able to conduct effective demonstration of images for the referring clinicians. The recent technological advances have given the radiologists an invaluable teaching and demonstration tool: the ability to manipulate CT and MR acquisitions in three dimensions. This method is ideally suited for instruction in cardiac anatomy and pathology. The heart is a complex structure, which does not respect the usual x, y, and z axes, choosing instead an orientation at various angles off the axial, coronal, and sagittal planes. In patients with cardiac diseases, the disease processes themselves, as well as intrinsic compensatory mechanisms to maintain homeostasis result in chamber dilatation, wall thickening or thinning, and displacement or rotation of the heart and great vessels. Recognition of these changes is the basis for cardiac diagnosis.

Multidetector CT imaging during administration of a bolus of intravenous contrast results in a data set containing the heart and the lungs in their "natural environment". The contrast-enhanced images are acquired on a GE Lightspeed multidetector CT scanner and reconstructed with 1.25 mm thickness with 0.6mm intervals. The data is then transferred to the Vitrea workstation and reconstructed in the body and cardiac axes with 50mm thick slabs, at 1mm intervals. The result is a volume of anatomic data, presented to the viewer in an intuitive three-dimensional format (dissection-like), where the spatial relationships of the organs are underscored continuously. The need to go up and down serial axial images is obviated by the volumetric nature of the presentation.

In this tutorial we present our approach to teaching normal anatomy and variants, as well as some pathologic entities, using 3-d volumetric reconstructions on a Vitrea work station. Computer reconstruction and multiplanar reformatting of this data set allows direct demonstration of the relationships among

their constituent parts. That is, the cardiac chambers, valves, the coronary arteries and the great vessels and their branches and tributaries are depicted explicitly. Conventional mental manipulation of these data sets in the head of the observer is no longer necessary. In addition, that which was previously reconstructed only in the observer's head is now explicitly available to the radiology residents and referring physicians.

The volumetric presentation of the data results in relative degradation of detail, and therefore cannot be used for diagnostic purposes without the axial source images. For example, in the case of cardiovascular system, distinguishing segmental pulmonary arteries from pulmonary veins is best achieved on the conventional axial thin section reconstructions. However, the volumetric 3-d data sets are invaluable for teaching gross anatomy and pathology. For the first time since Michelangelo we have in our hands a three-dimensional substitute for the dissection laboratory.

Instant display of the reconstructed data on the Vitrea workstation, which becomes the substrate for clinical interpretation, is now immediately available for view and analysis. In this presentation we display the heart and great vessels in their natural format, and demonstrate the normal heart and coronary arteries as they appear in life. In particular, we emphasize the left-to-right relationship of the mitral and tricuspid valves, the superior and inferior relationship of the left and right atria, and the left-to-right relationship of the pulmonary artery and aorta. Separation of the tricuspid and pulmonary valves, and fibrous continuity between the mitral and aortic valves are demonstrated. The origins and the course of the epicardial coronary arteries, as well as their relationship to other cardiac structures, are displayed. Recognition of the "natural" anatomy of the heart will form the basis for understanding tomographic anatomic representation in CT, echo, MRI, as well as the projection techniques, including plain chest radiography.

MRI of Congenital Heart Disease

Gautham P. Reddy, MD, MPH

The primary goal of imaging in congenital heart disease (CHD) is the precise demonstration of anatomy of the heart and great vessels. Because surgical repair and palliation of highly complex congenital cardiac lesions is now possible, exact depiction of the abnormalities is imperative.

Magnetic resonance imaging (MRI) has proven to be effective for morphologic assessment of CHD (1), and more recently for quantitative functional evaluation of the cardiovascular system (2,3). Its advantages over angiography are its non-invasive nature, its ability to depict extracardiac structures as well as the heart, its absence of radiation, and its lack of need for contrast media. Echocardiography is the primary non-invasive imaging technique used in CHD, mainly because it is widely available and because pediatric cardiologists are familiar with this modality. However, MRI has an important role as an alternative imaging technique and as an adjunct to echocardiography.

Techniques

The multislice spin echo MRI technique with electrocardiographic gating and respiratory compensation is optimal for accurate depiction of anatomy in patients with CHD. Transverse images from the aortic arch to the cardiac apex are usually obtained. On occasion short- or long-axis MR tomograms of the heart are acquired. The short-axis plane is defined from the long-axis view, which in turn is prescribed from the coronal or transverse planes. Coronal, sagittal, or oblique sequences can complement the transverse images. In general, 5 mm sections are used; however, thin (3 mm) slices are required for more detailed evaluation of conditions such as pulmonary artery stenosis and aortic coarctation. Gadolinium-enhanced MR angiography, performed in the sagittal plane during continuous intravenous administration of contrast agent, affords precise delineation of the thoracic aorta (4).

Cine MRI is composed of multiple gradient echo images obtained at different phases of the cardiac cycle. This technique can demonstrate abnormal flow in the heart and great vessels (5,6) permitting diagnosis of valvular stenosis or regurgitation, ventricular outflow stenosis, or shunting across septal defects. Cine MRI acquired through the ventricles allows assessment of ventricular contraction and function. In addition, cine MRI performed through the entire heart can be used for quantification of ventricular volumes and ejection fraction. Segmental K space

(“breath hold”) cine MRI can also be used to assess ventricular function. The velocity-encoded cine MRI technique allows measurement of blood flow velocity and volume in vessels and across shunts.

Specific Anomalies

Indications for MRI in CHD include anatomical and functional assessment before surgery and in the post-operative period. The most important clinical indications are: (A) delineation of anatomy in patients with situs abnormalities; complex ventricular anomalies; or abnormalities of the pulmonary arteries, pulmonary veins, systemic veins, or thoracic aorta; (B) quantification of function, including estimation of right and left ventricular masses; appraisal of collateral blood flow and pressure gradients in coarctation; and differentiation of flow between right and left pulmonary arteries; (C) post-operative imaging, including demonstration of morphology and post-surgical complications; and functional evaluation, such as measurement of conduit blood flow and pressure gradients.

Situs Abnormalities

MRI displays the characteristic features of the atria and ventricles, thereby demonstrating the type of situs and ventricular loop. The atria are differentiated by the configurations of their appendages: the left atrial appendage is tubular and has a narrow ostium; the right atrial appendage is triangular, with a wider ostium. The inferior vena cava is almost invariably connected to the anatomic right atrium. The right ventricle can be identified most reliably by the presence of a muscular infundibulum between the tricuspid and semilunar valves. In the left ventricle, there is fibrous continuity between the atrioventricular and semilunar valves. Other distinguishing features of the right ventricle are its triangular shape, coarse trabeculations at the apical septum, and moderator band at the apex, in contrast to the oval shape and smooth apical septum of the left ventricle.

In situs solitus, the anatomic right atrium is located on the right, and the anatomic left atrium is on the left. There is a D-ventricular loop, with the anatomic right ventricle positioned to the right of the left ventricle. In situs inversus, the morphologic right (systemic venous) atrium is on the left, and the morphologic left (pulmonary venous) atrium is on the right. An L-ventricular loop is present, with the right ventricle located on the left side of the left ventricle.

Isomerism can be diagnosed readily with MRI by

demonstrating the symmetric relationship of the bronchi and pulmonary arteries (7). CHD is usually present in patients with isomerism; left-sided isomerism is associated with polysplenia syndrome, and right-sided isomerism with asplenia.

Abnormalities of Ventriculoarterial Connections

This class of anomalies includes transposition of the great arteries, double-outlet right and double-outlet left ventricle, and truncus arteriosus. MRI effectively delineates the morphology of these anomalies, including the connections of the ventricles to the great vessels and the relationship of the arteries to each other (1, 8-11).

Transposition of the Great Arteries

In complete transposition, transverse images reveal the aorta anterior and to the right of the main pulmonary artery. Transverse and coronal images show the aorta arising from the normally-situated right ventricle and the pulmonary artery from the left ventricle (D-ventricular loop). MRI depicts the thick walls and circular cavity of the right ventricle compared to the thinner wall and elliptical shape of the left ventricle, which are characteristic of d-transposition. Associated abnormalities such as a ventricular septal defect (VSD) or pulmonary stenosis also can be identified by MRI (10).

In corrected transposition (l-transposition, L-ventricular loop), the aorta is anterior and to the left of the pulmonary artery. Transverse and coronal MR images demonstrate the origin of the aorta from the anatomic right ventricle, which is connected to the left atrium and is located to the left of the left ventricle (12).

MRI can be employed in the post-operative assessment of patients who have undergone arterial switch (Jatene) procedure (11) or atrial baffle (Mustard or Senning) procedure (13). After arterial switch surgery, MRI can be used to demonstrate stenosis of the right or left pulmonary arteries, an occasional complication of this operation.

Double-Outlet Right Ventricle (DORV)

Transverse and coronal MR sections at the base of the heart demonstrate the characteristic parallel relationship of the aorta and the pulmonary artery, both of which originate from the right ventricle (14). Occasionally, the aorta arises anterior to the pulmonary artery. Transverse images reveal a circle of muscle separating the mitral valve from the aortic and pulmonary valves. Side-by-side rings of myocardium may be seen in the right ventricular outflow tract. The location and size of the VSD can also be evaluated on transverse tomograms.

When valvular or subvalvular pulmonic stenosis is present, DORV may be clinically and angiographically similar to tetralogy of Fallot. Transverse MR images can confirm the diagnosis of DORV by directly demonstrating a rim of muscle interposed between the aortic and mitral valves.

Truncus Arteriosus

Transverse, coronal, and sagittal scans depict a truncus positioned over both ventricles, straddling a VSD. Sagittal and coronal planes are employed to show the origins of the pulmonary arteries from the truncus. MRI can also provide additional pertinent information, such as the relative sizes of the ventricles.

In both truncus arteriosus and pulmonary atresia, a single great artery arises from the heart. The diagnosis of truncus can be excluded with transverse MRI by demonstrating a small infundibular chamber, which establishes the diagnosis of pulmonary atresia.

After surgical repair of the truncus with a Rastelli conduit, transverse and sagittal images can be used to identify stenoses at the anastomosis or in the central pulmonary arteries.

Tetralogy of Fallot and Pulmonary Atresia

An anteriorly located aorta overriding a perimembranous VSD, infundibular pulmonic stenosis, small pulmonic annulus, and right ventricular hypertrophy are the features of tetralogy of Fallot. Sagittal and transverse MR tomograms depict the narrowed right ventricular outflow region, the ventricular septal defect, and the relative sizes of the aorta and the main pulmonary artery (1,15).

Because it does not require opacification of the pulmonary arteries with contrast material, MRI (with thin transverse slices) is the definitive method for ascertaining the existence of central pulmonary arteries and of a central confluence of the right and left pulmonary arteries in patients who have pulmonary atresia with VSD. MRI is the favored modality for imaging pulmonary arterial stenoses, which occur commonly in tetralogy. These stenoses are optimally evaluated with oblique planes parallel to the pulmonary arteries. Pulmonary arteries can sometimes be more easily visualized on cine MRI than on a spin-echo sequence.

Transverse tomograms in patients with this anomaly reveal a continuous band of myocardium in the right ventricular outflow tract, reflecting infundibular obstruction (16,17). The atresia can be focal (valvular only), or it may involve a longer segment. Focal membranous pulmonary atresia may be difficult to distinguish from critical stenosis on spin echo imaging, and

cine MRI can be used to establish whether there is flow across the valve. Pulmonary atresia can be divided into two groups based on the presence or absence of a VSD.

Pulmonary atresia with VSD is a severe form of tetralogy of Fallot. The aorta overrides the VSD in this form of pulmonary atresia. The pulmonary arteries are often stenotic, hypoplastic, or atretic; one of the principal advantages of MRI in these patients is the ability to assess the central pulmonary arteries distal to the atresia. Transverse scans determine the presence and length of atresia in the infundibulum and in the main pulmonary artery. However, stenoses and atresia in the left and right pulmonary arteries are best defined with oblique imaging planes parallel to these vessels. Collateral blood supply to the lungs can be demonstrated by MRI, most effectively by gradient echo images.

In patients who have pulmonary atresia with intact ventricular septum, the pulmonary arteries are generally normal or almost normal in caliber, without stenoses. The appearance of the right ventricle is variable, from marked hypoplasia to dilatation; transverse and sagittal sections are well-suited for the evaluation of right ventricular size.

MRI is effective for the pre-operative evaluation of the size of the central pulmonary arteries and the presence of a central confluence, factors that influence the decision to perform a Rastelli procedure. After surgery, MRI can be employed to depict surgical shunts and their anastomoses. The condition of the pulmonary arteries is ideally evaluated by MR images in the transverse and oblique (parallel to the left and right pulmonary arteries) planes.

Complex Ventricular Anomalies

A number of papers have shown the value of MRI in the evaluation of complex cyanotic heart disease (7, 18-21). Transverse images can readily delineate situs, location of the cardiac apex, type of bulboventricular loop, and relationship of the great arteries (18-20). In patients with splenic and heterotaxy syndromes, MR images of the upper abdomen demonstrate absence of the spleen (asplenia) or the presence of multiple small spleens (polysplenia). MRI also displays interruption of the inferior vena cava (polysplenia) or bilateral superior venae cavae (more common in asplenia).

MRI is capable of differentiating complex ventricular anomalies, which are sometimes difficult to distinguish by angiography. Two studies have shown the advantages of MRI compared to angiography in assessment of complex anomalies (18,19). These abnormalities include single ventricle of the double-inlet type; atresia of an atrioventricular valve with

hypoplasia of its respective ventricle; common atrioventricular valve; and common ventricle (absent ventricular septum). MRI demonstrates the size of the VSD, the thickness of the septum, the dimensions of the ventricles, connections of the atrioventricular valves, and the ventriculoarterial connections.

Left-to-Right Shunts

Ventricular Septal Defect

Spin-echo MRI can demonstrate VSDs with an accuracy of greater than 90% (22). Transverse tomograms are especially helpful because they demarcate the inflow and outflow regions of the ventricular septum (23).

A perimembranous VSD, the most common type, is identified on transverse images below the aortic root. VSDs of the inlet septum, associated with endocardial cushion defect (also known as atrioventricular canal), are readily identified by MRI (24). The other constituents of the endocardial cushion defect, an ostium primum atrial septal defect and a common atrioventricular valve, also can be visualized on transverse scans. Transverse, coronal, and sagittal MR tomograms depict defects that involve the outlet septum, such as subpulmonic VSDs and malalignment VSDs, which are associated with tetralogy of Fallot, truncus arteriosus, and DORV. The size of the VSD is shown clearly on transverse images.

Infracristal and supracristal defects can be distinguished using short-axis or transverse sections through the right ventricular outflow tract. Identification of myocardium between the pulmonic valve and the VSD is diagnostic of an infracristal VSD. Lack of muscle indicates a supracristal VSD (25).

Atrial Septal Defect

MRI can identify and precisely define the location of an atrial septal defect (ASD). Diagnosis of an ASD is considered definitive if the defect is seen on two consecutive transverse tomographic sections or if it is observed during several phases of the cardiac cycle at one anatomic level. The shunt across the ASD is depicted as a signal void with cine MR technique. One paper has reported greater than 90% sensitivity and specificity for MRI in the detection of ASD (26).

MRI depicts a sinus venosus ASD as absence of the portion of the atrial septum between the superior vena cava and the left atrium. MR images can also reveal anomalous pulmonary venous connection, which is associated with sinus venosus ASD. An advantage of MRI compared to echocardiography is the greater accuracy for demonstrating partial anomalous pulmonary venous connections. Secundum ASDs are displayed as defects in the center of the atrial septum.

The perimeter of the secundum defect is often thickened, a feature useful in distinguishing a true defect from signal loss due to septal thinning at the fossa ovalis. Transverse sections through the atrioventricular valve plane demonstrates a primum ASD as a defect in the inferior portion of the septum.

In patients with atrioventricular septal defect or atrioventricular canal (endocardial cushion defect), MRI shows a primum ASD, an inlet VSD, a common atrioventricular valve ring, and lack of a cardiac crux (24). Additional findings include elongation of the left ventricular outflow tract and shortening of the inlet ventricular septum. Spin echo MR images are usually unable to define the cleft mitral valve. Atrioventricular regurgitation associated with an atrioventricular septal defect can be identified and graded using cine MRI and velocity-encoded cine MRI.

Patent Ductus Arteriosus

MR imaging can readily depict a patent ductus arteriosus connecting the aorta and the pulmonary artery. Associated findings include dilatation of the aortic arch and focal aortic enlargement at the site of the ductus. However, even with thin (3 mm) sections, MRI might not detect a small ductus, especially in infants.

Pulmonary Venous Abnormalities

MRI is highly effective for evaluation of anomalous pulmonary venous connection. Partial anomalous pulmonary venous connection is associated with atrial septal defect, occurring in almost all patients with a sinus venosus ASD. Thus, pulmonary venous return must be delineated in patients with ASD (26,27). Transverse and coronal planes are best suited for this purpose. In the most common type of partial anomalous pulmonary venous connection, the right upper lobe pulmonary vein drains into the superior vena cava. A distended coronary sinus seen on transverse images may reflect partial anomalous connection. Scimitar syndrome can be diagnosed with MRI by identifying a common right pulmonary vein entering the inferior vena cava.

Absence of pulmonary veins emptying into the left atrium indicates total anomalous pulmonary venous connection. Depending on the site of anomalous connection, transverse tomograms may demonstrate a common pulmonary vein superior or posterior to the left atrium, an enlarged left superior vena cava, or a dilated coronary sinus.

Cine MRI is an excellent technique for evaluation of pulmonary varix. On spin echo images, however, visualization of the varix may be difficult due to its thin walls and lack of internal signal, which represents a flow void.

Systemic Venous Abnormalities

Thoracic systemic venous anomalies may have the appearance of a mediastinal mass on chest radiography. MRI is an ideal modality for confirming the presence of a venous abnormality and excluding a mass (28).

Persistent left superior vena cava is identified on transverse images. The left superior vena cava most frequently connects to the coronary sinus; the distended coronary sinus is easily seen on transverse scans. Occasionally, patients with asplenia syndrome may have an unroofed coronary sinus, in which the left superior vena cava drains directly into the right atrium.

Interruption of the inferior vena cava with azygous continuation is associated with polysplenia syndrome and complex congenital heart disease, although it can also occur in patients without congenital heart disease. The dilated azygous vein may mimic a posterior mediastinal mass on chest radiographs. MRI can effectively demonstrate the anatomy in this abnormality.

Thoracic Aortic Abnormalities

MRI is the technique of choice for imaging congenital anomalies of the thoracic aorta. Because it furnishes more information than angiography in most instances, MRI can usually replace the latter technique.

Aortic Arch Anomalies

MRI optimally demonstrates both the anatomy of aortic arch abnormalities (vascular rings) as well as airway compression, if present (29,30). Airway compromise is best seen on transverse and sagittal images.

The arch vessels are easily identified on MRI. Sagittal and transverse sections readily depict a retroesophageal subclavian artery. With a left aortic arch, an aberrant right subclavian artery generally has a normal caliber, and narrowing of the trachea or esophagus is unusual.

In patients with a right aortic arch, imaging in the transverse plane shows the arch on the right side of the trachea and the proximal descending aorta to the right of the spine. The descending thoracic aorta commonly crosses over to the left side, and transverse or coronal images clearly display the transition. If an aberrant left subclavian artery is present, its proximal segment is ordinarily dilated. This dilatation, known as a diverticulum of Kommerell, can compress the airway or the esophagus, resulting in symptoms. Sagittal MR tomograms can demonstrate this abnormal anatomy.

Double aortic arch is distinguished by the location of the trachea and esophagus between two vessels at

the level of the arch. MRI is ideal for visualizing these structures. Sagittal and transverse MR images display the dimensions of the two arches; the right arch is larger in approximately 80% of patients. During surgical repair, the smaller arch is usually ligated.

Coarctation of the Aorta

MRI is well suited for evaluation of aortic coarctation, the most common congenital abnormality of the thoracic aorta (31). Thin sections in the transverse, sagittal, and oblique sagittal (parallel to the arch) planes are highly accurate in defining the site of stenosis, the caliber of the distal arch, post-stenotic dilatation, and the relationship of arch vessels to the narrowed segment. Due to partial-volume averaging on transverse sections, the site of coarctation and its diameter and length are optimally depicted on sagittal and oblique sagittal images. Velocity-sensitive cine MR can be used to measure the pressure gradient across the coarctation site (32). Spin-echo MR images can reveal the presence of enlarged collateral channels, and velocity-encoded cine MRI is useful for quantifying the volume of collateral flow (33,34). Contrast-enhanced three-dimensional MR angiography is another technique for depiction of the coarctation as well as the presence of collateral vessels (4).

After repair of focal coarctation, MRI can be used to appraise the diameter of the aorta (32). In patients with long-segment stenosis, the status of aortic bypass grafts can be assessed by MR imaging. Spin echo technique can be employed to evaluate post-operative complications such as mediastinal hematoma and pseudoaneurysm formation. The outcome of balloon angioplasty, used to treat recurrence of coarctation, can also be demonstrated with MRI.

Functional Assessment of Congenital Heart Disease

Cardiovascular function in CHD can be evaluated with various MR imaging techniques, including cine MRI, breath hold (segmented K space) cine MRI, and velocity-encoded cine vascular phase contrast imaging.

To measure ventricular size and function, cine MRI is performed through the ventricles, and a volume of data is acquired for multiple phases of the cardiac cycle. The stacks of images obtained at end systole and end diastole can be used to quantify ventricular mass and volume and stroke volume (SV) ($SV = \text{end systolic volume} - \text{end diastolic volume}$). Ejection fraction ($SV/\text{end diastolic volume}$), the most useful measure of ventricular function, can also be calculated (35-37)

On cine MR images, flow voids can indicate valvular regurgitation or jet flow across a stenotic valve.

Regurgitant volume in aortic or mitral insufficiency can be calculated by subtracting right ventricular SV from left ventricular SV; for pulmonic or tricuspid regurgitation, left ventricular SV is subtracted from right ventricular SV (38).

Cine MRI provides two ways to quantify shunts. In the first method, right and left ventricular SVs are measured (6). In the absence of a shunt, the ventricles have equal SVs (35). With a left-to-right shunt at the atrial level (ASD or partial anomalous pulmonary venous connection), right ventricular SV exceeds left ventricular SV by the volume of the shunt. If a left-to-right shunt is due to a VSD or a patent ductus arteriosus, left ventricular SV will exceed right ventricular SV. The second technique uses velocity-encoded cine MRI to quantify blood flow in the ascending aorta and in the main pulmonary artery (2,39). Normally, flow is equal in these two arteries. In the presence of a left-to-right shunt in patients with atrial septal defect, partial anomalous pulmonary venous connection, or ventricular septal defect, blood flow in the pulmonary artery exceeds flow in the aorta by the quantity of the shunt. With a patent ductus arteriosus, aortic blood flow is greater than pulmonary flow. The opposite relationships are true for right-to-left shunts.

Velocity-encoded cine MRI is used to quantify blood flow in the central vessels (2,3). Ideally, the vessel of interest is scanned in a plane perpendicular to the flow direction using a phase contrast sequence. Flow velocity is calculated using a formula in which velocity is proportional to change in phase angle of protons in motion. Mean blood flow is estimated by multiplying mean velocity and the cross sectional area of the vessel.

Collateral flow in coarctation of the aorta can be measured with velocity-encoded cine MRI (33,34). Volume of flow is determined at two sites in the aorta: just beyond to the coarctation and at the level of the diaphragm. In the normal individual, the volume of blood flow is lower in the distal aorta. However, patients with coarctation may have higher flow distally, indicating retrograde collateral blood flow into the aorta via the intercostal arteries and the branches of the subclavian arteries.

Velocity-encoded cine MRI has the distinctive capability of determining blood flow separately in the left and right pulmonary arteries (40). This technique can also be used to estimate pressure gradients across stenoses of pulmonary arteries or surgical shunts (41) and across aortic coarctations (32).

Evaluation of the Postoperative Patient

As operative repair of CHD becomes more sophisticated and highly successful even for complex

anomalies, precise imaging is crucial for monitoring post-surgical patients. MRI is an ideal modality for evaluating these patients (18). Because it can readily define extracardiac anatomy, MRI is most effective in assessing patients who have undergone supracardiac surgery. Such operations, involving shunts or anastomoses above the heart, include systemic-to-pulmonary artery conduits; and the Jatene, Damas, Rastelli, Norwood, and Fontan procedures (11,18,42,43). MR imaging is also useful in monitoring individuals who have had intracardiac procedures. Intracardiac operations that can be evaluated by MRI include right ventricular outlet repair in tetralogy of Fallot; Mustard and Senning reconstructions (14,44); and intraventricular baffles for correction of double outlet right ventricle.

MRI readily demonstrates post-surgical complications such as anastomotic stricture, closure, or pseudoaneurysm; pulmonary artery stenosis or distortion (45); and hematoma, lymphocele, or seroma.

Velocity-encoded cine MRI is used for functional evaluation of the post-operative patient to evaluate shunt patency and flow (41), to estimate pressure gradients across anastomoses and stenotic vessels (32,41), to assess flow dynamics (46), to quantify blood flow in the pulmonary arteries (40), and to calculate the volume of pulmonic regurgitation after repair of tetralogy of Fallot (47).

REFERENCES

1. Didier D, Higgins CB, Fisher M, Osaki L, Silverman N, Cheitlin M: Congenital heart disease: gated MR imaging in 72 patients. *Radiology* 1986;158:227-235.
2. Szolar DH, Hajime S, Higgins CB: Cardiovascular applications of magnetic resonance flow and velocity measurements. *JMRI* 1996;1:78-89.
3. Mohiaddin RH, Longmore DB: Functional aspects of cardiovascular NMR imaging. *Circulation* 1993;88:264-281.
4. Prince MR, Narasimham DC, Stanley JC, et al.: Breath hold gadolinium angiography of the abdominal aorta and its major branches. *Radiology* 1995;197:785-792.
5. Sechtem U, Pflugfelder PW, White RD, Gould RG, Holt W, Lipton MJ, Higgins CB: Cine MRI: Potential for the evaluation of cardiovascular function. *AJR* 1987;148:239-246.
6. Sechtem U, Pflugfelder P, Cassidy MC, Holt W, Wolfe C, Higgins CB: Ventricular septal defect: visualization of shunt flow and determination of shunt size by cine magnetic resonance imaging. *AJR* 1987;149:689-691.
7. Wang J-K, Li Y-W, Chiu I-S, et al.: Usefulness of MRI in the assessment of venoatrial connections, atrial morphology, bronchial situs, and other anomalies in right atrial isomerism. *Am J Cardiol* 1994;74:701-704.
8. Higgins CB, Silverman N, Kersting-Sommerhoff B, Schmidt K: *Echocardiography and MRI of Congenital Heart Disease*. New York: Raven Press, 1990.
9. Higgins CB, Byrd BF, III, Farmer DW, Osaki L, Silverman NH, Cheitlin MD: Magnetic resonance imaging in patients with congenital heart disease. *Circulation* 1984;70:851-860.
10. Guit GL, Bluemm R, Rohmer J, Wenink AC, Chin JG, Doornbos J, van Voorthuisen E: Levotransposition of the aorta: identification of segmental cardiac anatomy using MR imaging. *Radiology* 1986;161:673-6
11. Blankenberg F, Rhee J, Hardy C, Higgins CB: Contribution of MRI to the evaluation of the Jatene procedure in comparison to echocardiology. *J Comput Assist Tomogr* 1994;18:749-754.
12. Reddy GP, Caputo GR: Congenitally corrected transposition of the great arteries. *Radiology* 1999; 213:102-106.
13. Thiessen P, Kaemmerer H, Sechtem U, et al.: MRI of cardiac function and morphology in patients with transposition of great arteries following Mustard procedure. *Thorac Cardiovasc Surg* 1991;39(Suppl 3):221-224.
14. Mayo JR, Roberson D, Sommerhoff B, Higgins CB: MRI of double outlet right ventricle. *J Comput Assist Tomogr* 1990;14:336-339.
15. Mirowitz SA, Gutierrez FR, Canter CE, Vannier MW: Tetralogy of Fallot: MR findings. *Radiology* 1989;171:207-212.
16. Gomes AS, Lois JF, Williams RG: Pulmonary arteries: MR imaging in patients with congenital obstruction of the right ventricular outflow tract. *Radiology* 1990;174:51-57.
17. Kersting-Sommerhoff BA, Sechtem U, Higgins CB: Evaluation of pulmonary blood supply by nuclear magnetic resonance imaging in patients with pulmonary atresia. *JACC* 1988;11:166-171.
18. Kersting-Sommerhoff BA, Diethelm L, Stanger P, Dery R, Higashino SM, Higgins SS, Higgins CB: Evaluation of complex congenital ventricular anomalies with magnetic resonance imaging. *Am Heart J* 1990;120:133-142.
19. Peshok RM, Parrish M, Fixler D, Parkey RW: Magnetic resonance imaging of single ventricle. *Circulation* 1985; 72(suppl III):29.
20. Jacobstein MD, Portman MA, Fletcher BD: Magnetic resonance imaging in univentricular atrioventricular connection. *Am J Cardiac Imaging* 1987;1:221-226.
21. Geva T, Vick W, Wendt RE, Rokey R: Role of spin echo and cine MRI in presurgical planning of heterotaxy syndrome. *Circulation* 1994;90:348-356.
22. Kersting-Sommerhoff BA, Diethelm L, Teitel DF, Sommerhoff CB, Higgins SS, Higashino SS, Higgins CB: Magnetic resonance imaging of congenital heart disease: sensitivity and specificity using receiver operating characteristic curve analysis. *Am Heart J* 1989;118:155-162.
23. Didier D, Higgins CB: Identification and localization of ventricular septal defects by gated magnetic resonance imaging. *Am J Cardiol* 1986;57:1363-1368.
24. Parsons JM, Baker EJ, Anderson RH, et al.: Morphological evaluation of atrioventricular septal defects by MRI. *Br Heart J* 1990;64:138-145.
25. Bremerich J, Reddy GP, Higgins CB: MRI of supracristal ventricular septal defects. *J Comput Assist Tomogr* 1999; 23:13-15.
26. Diethelm L, Dery R, Lipton MJ, Higgins CB: Atrial level shunts: sensitivity and specificity of MR in diagnosis. *Radiology* 1987;162:181-186.
27. Masui T, Seelos KC, Kersting-Sommerhoff BA, Higgins

- CB: Abnormalities of the pulmonary veins: evaluation with MR imaging and angiography and echocardiography. *Radiology* 1991;181:645-649.
28. Fisher MR, Hricak H, Higgins CB: Magnetic resonance imaging of developmental venous anomalies. *AJR* 1985;145:705-709.
 29. Bisset GS III, Strife JL, Kirks DR, Bailey WW: Vascular rings: MR imaging. *AJR* 1987;149:251-256.
 30. Kersting-Sommerhoff BA, Sechtem UP, Fisher MR, Higgins CB: MR imaging of congenital anomalies of the aortic arch. *AJR* 1987;149:9-13.
 31. von Schulthess GK, Higashino SM, Higgins SS, Didier D, Fisher MR, Higgins CB: Coarctation of the Aorta: MR imaging. *Radiology* 1986;158:469-474.
 32. Rees S, Somerville J, Warad C, Martinez J, Mohiaddin RH, Underwood R, Longmore DB: Coarctation of the aorta: MR imaging in late postoperative assessment. *Radiology* 1989;173:499-502.
 33. Steffens JC, Bourne MW, Sakuma H, Higgins CB: Quantitation of collateral blood flow in coarctation of the aorta by velocity encoded cine MRI. *Circulation* 1994;90:937-943.
 34. Reddy GP, Bremerich J, Higgins CB. Determination of the functional significance of coarctation of the aorta using velocity-encoded cine MRI. *Radiology* 1999; 213(P):220.
 35. Sechtem U, Pflugfelder PW, Gould RG, Cassidy MM, Higgins CB: Measurement of right and left ventricular volumes in healthy individuals with cine MR imaging. *Radiology* 1987;163:687-702.
 36. Semelka RC, Tomei E, Wagner S, Mayo J, Kondo C, Suzuki J-I, Caputo G, Higgins CB: Normal left ventricular dimensions and function: Interstudy reproducibility of measurements with cine MR imaging. *Radiology* 1990;174:763-768.
 37. Semelka RC, Tomei E, Wagner S, Mayo J, Caputo G, O'Sullivan M, Parmley WW, Chatterjee K, Wolfe C, Higgins CB: Inerstudy reproducibility of dimensional and functional measurements between cine magnetic resonance studies in the morphologically abnormal left ventricle. *Am Heart J* 1990;119:1367-1373.
 38. Sechtem U, Pflugfelder PW, Cassidy MM, White RD, Cheitlin MD, Schiller NB, Higgins CB: Mitral or aortic regurgitation: Quantification of regurgitant volumes with cine MR imaging. *Radiology* 1988;167:425-430.
 39. Brenner LD, Caputo GR, Mostbeck G, Steiman D, Dulce M, Cheitlin MD, O'Sullivan M, Higgins CB: Quantification of left to right atrial shunts with velocity encoded cine nuclear magnetic resonance imaging. *J Am Coll Cardiol* 1992;20:1246-1250.
 40. Caputo GR, Kondo C, Masui T, Geraci SJ, Foster E, O'Sullivan M, Higgins CB: Determination of right and left lung perfusion with oblique angle velocity encoded cine MR imaging: in vitro and in vivo validation. *Radiology* 1991; 180:693-698.
 41. Martinez JE, Mohiadden RH, Kilner DJ, et al.: Obstruction in extracardiac ventriculopulmonary conduits: value of NMR imaging with velocity mapping and Doppler echocardiography. *J Am Coll Cardiol* 1992;20:338-344.
 42. Jacobstein MD, Fletcher BD, Nelson AD, et al: Magnetic resonance imaging: evaluation of palliative systemic-pulmonary artery shunts. *Circulation* 1984;70:650-656.
 43. Julsrud PR, Ehman RL, Hagler DJ, Ilstrup DM: Extracardiac vasculature in candidates for Fontan surgery: MR imaging. *Radiology* 1989;173:503-506.
 44. Sampson C, Kilner PJ, Hirsch R, et al.: Venoatrial pathways after the Mustard operation for transposition of the great arteries: Anatomic and functional MR imaging. *Radiology* 1994;193:211-217.
 45. Duerinckx AJ, Wexler L, Banerjee A, Higgins SS, Hardy CE, Helton G, Rhee J, Mahboubi S, Higgins CB: Postoperative evaluation of pulmonary arteries in congenital heart surgery by MR imaging: Comparison with echocardiography. *Amer Heart J* 1994;128:177-184.
 46. Rebergen SA, Ottenkamp J, Doornbos J, et al.: Post-operative pulmonary flow dynamics after Fontan surgery: assessment with NMR velocity mapping. *J Am Coll Cardiol* 1993;21:123-131.
 47. Rebergen SA, Chin JGJ, Ottenkamp J, et al.: Pulmonary regurgitation in the late postoperative followup of tetralogy of Fallot. Volumetric quantitation by NMR velocity mapping. *Circulation* 1993;88:2257-2266.

Pericardial Imaging

Lynn S. Broderick, MD
University of Wisconsin-Madison

Objectives

After attending the lecture “Pericardial Imaging”, the attendee should be able to:

1. Describe the anatomy of the pericardium, including pericardial recesses.
2. Describe developmental abnormalities of the pericardium and their imaging findings.
3. Describe etiologies of pericardial effusion and radiographic and cross-sectional imaging findings.
4. Describe the diagnostic criteria for the diagnosis of constrictive pericarditis.
5. Describe pericardial neoplasms and their imaging findings.

Anatomy

The pericardium is made up of two layers, the serous visceral layer, also known as the epicardium, which is adherent to the heart, and the fibrous parietal layer, which is attached to the great vessels and central tendon of the diaphragm. The pericardial space lies between these two layers and normally contains 20-25 ml of fluid. The pericardium can be identified on the radiograph as well as CT and MR images if outlined by sufficient subepicardial and anterior mediastinal fat. Normally the pericardium is only 1-2 mm thick. The pericardium extends superiorly to cover the anterior aspect of the aorta at the level of the aortic arch.

Pericardial Defect

Congenital pericardial defects are uncommon and occur more frequently in males. Usually, there is only a partial defect and it most commonly occurs on the left. Although patients are often asymptomatic, herniation of the cardiac structures through the defect can occur resulting in death. This is more likely to occur in smaller defects than in larger defects. Most patients (75%) with a pericardial defect will also have a parietal pleural defect. Up to one third of patients will have other accompanying congenital abnormalities. A partial pericardial defect can be suspected on chest radiograph when there is bulging of the cardiomedial silhouette at the level of the main pulmonary artery and the left atrial appendage. If there is complete absence of the left pericardium, the chest radiograph shows the heart is shifted to the left, with a flattened left heart border. There is a long

prominent pulmonary artery segment and lung is interposed between the cardiac apex and the diaphragm. CT can demonstrate the abrupt termination of the pericardium. Aerated lung may be interposed between the main pulmonary artery and the ascending aorta. The sternopericardial ligament will be absent. If the patient is placed in the left lateral decubitus position, the heart will shift to lie against the left chest wall.

Acquired pericardial defects are usually post-surgical but can also recur as a result of trauma or peptic ulcer disease eroding into the pericardium. The most common post-surgical defect occurs following coronary artery bypass surgery. Because the incision is linear and lies beneath the sternum, there is usually complete healing of the defect. The presence of a surgical pericardial defect can be made by noting discrete bulge in the cardiac silhouette or abnormal passage of fluid or gas between the pericardium and the pleural space. Acute cardiac herniation can occur following surgery, usually in the first 24 hours. It is often preceded by a change in patient position or manipulation such as suctioning and coughing.

Pericardial Cysts

Most pericardial cysts are actually pleuropericardial cysts. They are most commonly located in the right cardiophrenic angle although they can occur anywhere along the pericardium. They occur in males more frequently than females. Usually patients are asymptomatic and the cyst is an incidental finding. On chest radiograph, pericardial cysts appear as focal areas of increased opacity, usually at the right cardiophrenic angle. On lateral view there will be increased density overlying the heart. CT and MR will demonstrate the cystic nature of these lesions and their direct relation to the pericardium. Prominent pericardial fat may give a similar appearance. CT and MR will demonstrate the fatty nature of the mass and exclude a soft tissue mass.

Pneumopericardium

The most common cause of pneumopericardium is trauma. This is usually post-surgical but can also occur as a result of blunt or penetrating trauma or barotrauma. Pneumopericardium has also been reported as a result of tumor, infection or gastric or duodenal ulcers eroding through the pericardium.

Pericardial Fluid

The causes of pericardial effusion are quite numerous. It can be difficult to detect pericardial effusions of less than 200 cc on chest radiograph. With larger pericardial effusion, the cardiac silhouette enlarges and often forms a globular shape. If the subepicardial fat is separated from the mediastinal fat by more than 2 mm, it indicates that pleural thickening or fluid is present. Absence of this sign, however, does not exclude the presence of pericardial disease. The displaced fat sign was first reported on the posteroanterior view but is more commonly seen on the lateral view. Although echocardiography is most commonly used for evaluation of possible pericardial effusion, it can be easily detected with CT and MR. Knowledge of the pericardial anatomy is important in distinguishing small collections of fluid within the pericardial recesses from lymphadenopathy or other pathology. The superior pericardial recess extends anteriorly and superiorly to cover the main pulmonary artery and the ascending aorta to the level of the left brachiocephalic vein. It extends along the right side of the ascending aorta and is in direct continuity with the transverse recess. The transverse recess is often crescentic in shape and lies just posterior to the ascending aorta. Knowledge of its location and typical appearance will prevent it being confused with adenopathy. The oblique pericardial sinus lies immediately posterior to the left atrium. There is also a left pulmonary recess located between the left pulmonary artery and left superior pulmonary vein, a postcaval recess between the superior vena cava and the right pulmonary artery and right superior pulmonary vein and a pulmonary venous recess, located between the superior and inferior pulmonary veins.

Dressler syndrome is a condition originally described in patients following myocardial infarction. It can also occur following heart surgery and may be better termed postpericardiotomy syndrome. The patient develops fever, myalgias, and chest pain and has a pericardial friction rub. Chest radiograph shows pleural effusion. Pericardial effusion can be suspected on chest radiograph or documented by echocardiography.

Constrictive Pericarditis

Constrictive pericarditis occurs when there is pericardial thickening and/or calcification that prevents the normal filling of the cardiac chambers. Patients present with dyspnea, peripheral edema and ascites. On echocardiography, there is elevation of the diastolic filling pressures. However, these findings may be present in patients with constrictive pericarditis or restrictive cardiomyopathy. Echocardiography does

not reliably assess the pericardium and so these patients are often referred for CT or MR imaging. Although CT and MR can reliably assess for pericardial thickening, CT better depicts areas of calcification. Rienmüller, et al, described the CT findings of constrictive pericarditis. They include pericardial thickening and/or calcification, narrowing of the heart at the level of the atrioventricular groove, enlargement of the atrium or atria, and dilatation of the superior vena cava (greater than or equal to the size of the descending aorta) or inferior vena cava (greater than or equal to twice the size of the descending aorta). Oftentimes, the cause of the constrictive pericarditis is unknown. It may occur as a result of infection, connective tissue disease, neoplasm, trauma, radiation injury, or uremia.

Pericardial Tumors

Metastatic disease is the most common cause of neoplastic involvement of the pericardium. Most patients with metastases to the pericardium will have evidence of metastases elsewhere in the body. The most common tumors to involve the pericardium secondarily are lung and breast cancer and lymphoma/leukemia. Although soft tissue nodules or masses can be demonstrated by cross-sectional imaging, effusion may be the only manifestation of pericardial metastases. Primary tumors of the pericardium include mesothelioma, sarcoma, lymphoma, teratoma and pheochromocytoma.

REFERENCES

1. Agner RC, Gallis HA. Pericarditis: differential diagnostic considerations. *Arch Intern Med* 1979; 139:407-412
2. Baron MG. Pericardial effusion. *Circ* 1971; 44:294-299
3. Bull RK, Edwards PD, Dixon AK. CT dimensions of the normal pericardium. *Brit J Radiol* 1998; 71:923-925
4. Burke A, Virmani R. Tumors of the heart and great vessels. In: *Atlas of tumor pathology*. Fasc 16, ser 3. Washington, DC: Armed Forces Institute of pathology, 1996
5. Carsky EW, Mauceri RA, Azimi F. The epicardial fat pad sign: analysis of frontal and lateral chest radiographs in patients with pericardial effusion. *Radiol* 1980; 137:303-308
6. Choe YH, Im JG, Park JH, et al. The anatomy of the pericardial space: a study in cadavers and patients. *Am J Roentgenol* 1987; 149:693-697
7. Delille JP, Hernigou A, Sene V, et al. Maximal thickness of the normal human pericardium assessed by electron-beam computed tomography. *Eur Radiol* 1999; 9:1183-1189
8. Galzer GM, Gross BH, Orringer MB, et al. Computed tomography of pericardial masses: further observations and comparison with echocardiography. *J Comput Assist Tomogr* 1984; 8:895-899
9. Groell R, Schaffler GJ, Rienmüller R. Pericardial sinuses and recesses: findings at electrocardiographically triggered electron-beam CT. *Radiol* 1999; 212:69-73

10. Hamilton BH, Francis IR, Gross BH, et al. Intrapericardial paragangliomas (pheochromocytomas): imaging features. *Am J Roentgenol* 1997; 168:109-113
11. Kralstein J, Frishman W. Malignant pericardial diseases: diagnosis and treatment. *Am Heart J* 1987; 111:785-790
12. Kremens V. Demonstration of the pericardial shadow on the routine chest roentgenogram: a new roentgen finding. *Radiol* 1955; 64:72-80
13. Levy-Ravetch M, Auh YH, Rubenstein WA. CT of the pericardial recesses. *Am J Roentgenol* 1985; 144:707-714
14. Masui T, Finck S, Higgins CB. Constrictive pericarditis and restrictive cardiomyopathy: evaluation with MR imaging. *Radiol* 1992; 182:369-373
15. Miller SW. Imaging pericardial Disease. *Radiol Clin N Am* 1989; 27:1113-1125
16. Paling MR, Williamson BRJ. Epipericardial fat pad: CT findings. *Radiol* 1987; 165:335-339
17. Sechtem U, Tscholakoff D, Higgins CB. MRI of the normal pericardium. *Am J Roentgenol* 1986; 147:239-244
18. Sechtem U, Tscholakoff D, Higgins CB. MRI of the abnormal pericardium. *Am J Roentgenol* 1986; 147:245-252
19. Takasugi JE, Godwin JD. Surgical defects of the pericardium: radiographic findings. *Am J Roentgenol* 1989; 152:951-954
20. Van Son JAM, Danielson GK, Schaff HV, et al. Congenital partial and complete absence of the pericardium. *Mayo Clin Proc* 1993; 68:743-747

MR Imaging in Right Ventricular Dysplasia

Joel E. Fishman, MD, PhD

Department of Radiology

University of Miami

Objectives

1. To review the clinical, imaging, and pathologic findings in arrhythmogenic right ventricular dysplasia (ARVD).
2. To describe the MR pulse sequences and techniques used in the evaluation of ARVD.
3. To review the published data regarding specific MR findings in ARVD and identify the problems faced in evaluating these images.

Introduction

ARVD was first described in 1977 by Fontaine, and consists of anatomic and functional abnormalities of the right ventricle leading to arrhythmias of right ventricular (RV) origin. In recent years, the name ARVC (for cardiomyopathy) has been suggested, because rather than being a developmental defect, it is increasingly evident that it is a progressive, non-ischemic atrophy of the RV myocardium. This condition is most often identified in adolescents and young adults, and is familial in 30-50% of cases (autosomal dominant); some investigators have identified abnormalities on multiple chromosomes. It is especially prevalent in northern Italians. The disease may be clinically silent; symptoms suggesting ARVD include palpitations and syncope or presyncope, particularly occurring during athletics. This reflects ventricular arrhythmias in an LBBB morphology, which can progress to VT or VF. Other electrocardiographic criteria include epsilon waves, QRS prolongation, and inverted T waves in the right precordial leads. Unfortunately many cases are only diagnosed after sudden cardiac death. Pathologically, there are two main variants of disease. The fatty form consists of replacement of RV myocardium by fat, primarily in the apical and infundibular regions, without wall thinning. The fibrofatty form includes fibrosis, usually with RV wall thinning (<3 mm), and dilatation of the RV and RV outflow tract (RVOT). Findings in both types can be focal or diffuse. Left ventricular involvement has been described in a variable percentage of cases.

There is an overlapping entity termed idiopathic right ventricular outflow tract tachycardia (RVOTT). This condition, often exercise-induced, is nonfamilial

and has a much lower risk of sudden cardiac death than does ARVD. However, there are similarities in the clinical and imaging features of this entity, and it may be a milder form of ARVD.

Diagnosis

Many criteria have been proposed for diagnosing ARVD, but it often remains problematic. An international study group has proposed criteria for diagnosis in six categories: family history, ECG depolarization abnormalities, ECG repolarization abnormalities, arrhythmias, biopsy, and global/regional dysfunction or structural alterations (by imaging). A definitive diagnosis of ARVD is made if endomyocardial biopsy shows full-thickness substitution of the RV wall by fatty or fibrofatty tissue. Biopsy can be hazardous, however, and can miss the diagnosis due to sampling error. Only the septum can be safely biopsied, a region that is relatively unaffected by ARVD. In practice relatively few patients are biopsied.

Imaging Findings

Using echocardiography and ventriculography, major imaging criteria for ARVD include severe dilatation and reduction of RV ejection fraction, localized RV aneurysms (akinetic or dyskinetic), and severe segmental dilatation of the RV. Minor criteria include milder RV dilatation (global/segmental) and regional RV hypokinesia. Neither of these methods can adequately assess the RV wall for fat or fibrosis.

MR Technique

MRI has become a major component of the evaluation algorithm for ARVD. It combines the functional capabilities required above with the potential to identify fatty infiltration or thinning of the RV wall. However, there are no current standards for the performance of MR in this setting. These studies can be difficult to perform, due to the presence of pulsation and respiration artifacts and the high frequency of arrhythmias. We prefer to use a surface coil with the patient prone in order to optimize SNR over the RV free wall. The axial plane generally yields the best quality images, but short axis or sagittal images are advisable to image the inferior RV wall. Most investigators perform black-blood imaging (non-breathhold

T1 and/or breathhold double IR), and cine gradient echo imaging for wall motion. We find that fat-suppressed black blood imaging yields better images of the RV wall than non-suppressed methods. Presaturation bands are very useful in the black-blood methods. We use a posterior band to suppress LV motion and aortic pulsation; this also permits using a rectangular field of view to shorten imaging time. Some centers use presaturation bands above and below the stack of images to suppress flow artifacts. The use of presaturation bands generally increases imaging time somewhat.

MR Findings in ARVD

MR findings of ARVD include abnormal myocardial signal intensity (high on standard, low on fat-suppressed images) consistent with fat in the RV wall. Wall thinning is commonly seen in the fibrofatty form. Both of these findings, however, can be difficult to make with assurance due to (1) the normally thin RV myocardium (3-4 mm, thinning even more towards the apex) and (2) being able to distinguish epicardial fat (normal) from fat within the wall itself. Identifying islands of fat within the wall, surrounded by myocardium, enhances accuracy. Increased right ventricular trabeculation has also been described as being associated with ARVD. Cine imaging is an important adjunct to the black-blood studies. The identification of wall motion abnormalities (either aneurysmal or diffuse or focal in the areas of wall thinning) increases suspicion for ARVD.

Despite the now widespread use of MRI in this setting, there has been relatively little quantitative analysis in the literature regarding sensitivity, specificity, and interobserver variation. In Auffermann's study from Germany, the most common abnormalities in patients with ARVD were focal abnormalities of RV morphology (78%), regional wall thinning (67%), and dilatation of the RVOT (33%). Increased signal in the RV wall suggesting fat was observed in 22%. They found agreement between MR findings and angiography in 86% of patients. In a study from Italy (Midiri et al), 14 of 30 patients (47%) with suspected ARVD had evidence of fatty infiltration; this

was the most frequent finding among their patients. Dilatation of the RV or RVOT was present in 43%. A French study showed an even higher (90%) prevalence of high signal intensity in the RV or RVOT in ten patients vs. ten controls (10%). Studies from the US have not shown similarly high rates of suspected fatty infiltration; this probably reflects many factors, especially disease prevalence and severity. In a study by White et al, of 46 patients with possible RVOTT (and believed not to have ARVD), 24 (52%) of patients had MR abnormalities of the RVOT and RV; 11(24%) had abnormalities of the RVOT only, and 11 (24%) were normal. Fatty infiltration was suggested in 25%. With the high rate of RV abnormalities, it may not be possible to distinguish ARVD and RVOTT by MRI. Because the diagnoses of ARVD and RVOTT can be problematic and without an accepted gold standard in many cases, MRI efforts should emphasize improving image quality and documenting a high level of interobserver agreement so as to provide maximal added benefit in evaluating for this disease.

REFERENCES

Blake LM, et al. MR features of arrhythmogenic right ventricular dysplasia. *AJR* 1992; 162:809-814.

Auffermann W. Wichter T. Breithardt G. et al. Arrhythmogenic right ventricular disease: MR imaging vs angiography. *AJR* 1993; 161:549-55.

Fuber A. Victor J. Merheb M. et al. Is the presence of right ventricular high intensity signals sufficient for the diagnosis of right ventricular dysplasia? *Archives des Maladies du Coeur et des Vaisseaux*. 1996; 89(9):1167-75.

Midiri M. Finazzo M. Brancato M. et al. Arrhythmogenic right ventricular dysplasia: MR Features. *Eur. Radiol.*1997; 7:307-312

Fontaine G. Arrhythmogenic right ventricular cardiomyopathies: clinical forms and main differential diagnoses. *Circulation* 1998;97:1532-1535.

Sommer T. Lewalter T. Bierhoff E. et al. MRI diagnosis of right ventricular dysplasia. *Rofo. Fortschritte auf dem Gebiete der Rontgenstrahlen* 1998; 169(6):609-15

White R. Trohman R. Flamm S. et al. Right Ventricular Arrhythmia in the Absence of Arrhythmogenic Dysplasia: MR Imaging of Myocardial Abnormalities. *Radiology* 1998;207:743-751.

Corrado D, Basso C, Thiene G. Arrhythmogenic right ventricular cardiomyopathy: diagnosis, prognosis, and treatment. *Heart* 2000;83:588-595.

Imaging the Patient with Pulmonary Hypertension

Aletta Ann Frazier, MD

Robert M. Steiner, MD

Objectives of This Presentation

1. To place pulmonary hypertension within a conceptual framework of pre-capillary (arterial) and post-capillary (venous) disease conditions.
2. To understand the histopathologic features, clinical presentation, current treatment, and long-term prognosis of the idiopathic and secondary conditions which produce pulmonary hypertension.
3. To recognize the classic radiologic manifestations of pre-capillary and post-capillary pulmonary hypertension, and also the potentially distinguishing imaging features which may assist in the differential diagnosis of pulmonary hypertension.
4. To consider an algorithm for the diagnosis and follow-up of clinically suspected pulmonary hypertension.

Pulmonary Hypertension

Pulmonary hypertension is hemodynamically defined as a mean pulmonary artery pressure greater than 25 mm Hg at rest or greater than 30 mm Hg during exercise, with increased pulmonary vascular resistance. The diagnosis is made by clinical assessment of hemodynamic parameters, medical history, and histologic findings. Pulmonary hypertension is the consequence of vascular changes within the arterial (pre-capillary) or venous (post-capillary) pulmonary circulation. These changes may be idiopathic, as in primary pulmonary hypertension or pulmonary veno-occlusive disease, but more commonly they represent a secondary response to alterations in pulmonary blood flow. The well-recognized etiologies of pre-capillary pulmonary hypertension include longstanding cardiac left-to-right shunt, chronic interstitial lung disease, chronic thromboembolic disease, and widespread pulmonary embolism arising from intravascular malignant cells, parasites or inorganic foreign materials. Post-capillary pulmonary hypertension develops when pulmonary venous drainage is compromised, most often due to left ventricular failure, left atrial neoplasia, mitral stenosis, focal venous constriction, or anomalous pulmonary venous connections.

The histologic changes of pre-capillary pulmonary hypertension are chiefly found in the walls of the

muscular arteries. Findings include intimal cellular proliferation and medial smooth muscle hypertrophy. Necrotizing arteritis and plexiform lesions are additional histologic features exclusively found in PPH and cases of left-to-right congenital cardiac shunt. Regarded by cardiovascular pathologists as the hallmark of sustained and irreversible pulmonary arterial hypertension, the plexiform lesion is a focal disruption of the internal elastic lamina by a “glomeruloid” plexus of endothelial channels which have ramified into alveolar septal capillaries. Complications of pre-capillary pulmonary hypertension include central arterial thrombosis, premature atherosclerosis of central elastic and muscular pulmonary arteries, aneurysmal dissection of pulmonary arteries, pulmonary infarction, and hypertrophy and dilatation of the right heart.

The histologic findings of post-capillary pulmonary hypertension are medial hypertrophy and intimal proliferation of the pulmonary veins. Typically there is marked prominence of the venous internal elastic lamina. The unique histologic hallmark of pulmonary veno-occlusive disease (PVOD) is the additional presence of webs, recanalized thrombosis and intimal fibrosis within pulmonary veins. The complications of post-capillary pulmonary hypertension include capillary congestion (with adjacent vascular proliferation), intra-alveolar hemosiderin deposition, interlobular septal edema, and septal fibrosis. Paraseptal venous infarcts may occur adjacent to a complete venous occlusion, particularly when markedly elevated pulmonary venous pressure is present.

Clinical Overview: Pre-capillary Pulmonary Hypertension

Primary pulmonary hypertension (PPH) remains an enigmatic condition which creates a hemodynamic pattern of elevated right atrial and mean pulmonary arterial pressures, normal pulmonary-capillary wedge pressures, and decreased cardiac output. Patients present with progressive dyspnea (60%), fatigue, angina, syncope, cor pulmonale and/or Raynaud’s phenomenon. Women are affected three times as often as men. Patients with portal hypertension, collagen vascular disease, or human immunodeficiency virus infection have an increased risk of developing PPH although no direct causal link has been established.

Therapeutic agents include vasodilators, calcium channel blockers, anticoagulants and diuretics to counteract the unfavorable hemodynamics. Lung or combined heart-lung transplantation may be performed. The majority of patients succumb 2 to 5 years following diagnosis.

The radiologic manifestations of PPH include prominent central pulmonary arteries, sharply tapering peripheral vessels, and right ventricular enlargement. Computed tomography (CT) demonstrates right ventricular hypertrophy, enlargement of central pulmonary arteries, and abruptly diminished peripheral vascularity. A CT-determined mean PA diameter of ≥ 29 mm demonstrates 87% sensitivity and 89% specificity for predicting pulmonary hypertension. Specificity climbs to 100% when a mean PA diameter of ≥ 29 mm is accompanied by findings of a segmental artery-to-bronchus ratio of $>1:1$ in three of four pulmonary lobes. When the ratio of CT-determined pulmonary artery diameter to aortic diameter is greater than one ("rPA > 1 "), a strong correlation with elevated mean pulmonary artery pressure has been shown, particularly in patients less than 50 years of age. On high-resolution CT (HRCT), both idiopathic and secondary forms of pulmonary hypertension may produce a mosaic pattern of lung attenuation, suggesting regional variations in parenchymal perfusion. Arteriography demonstrates symmetrically enlarged central arteries with pruned subsegmental vessels, filamentous peripheral arteries, and subpleural collaterals. Magnetic resonance (MR) imaging of patients with pulmonary hypertension reveal central pulmonary arterial dilatation, right ventricular hypertrophy, and reversal of septal curvature. Gated spin-echo MR images have shown abnormal intravascular signal corresponding to slow pulmonary arterial blood flow, notably with a direct relationship to elevated pulmonary vascular resistance.

Patients with sustained congenital cardiac left-to-right shunt who develop secondary pulmonary hypertension have shown adaptive anastomotic pathways which connect pulmonary arterial vessels (containing plexiform lesions) to bronchial arteries located within terminal bronchioles and the vasa vasora of pulmonary arteries. In such unusual cases when a congenital cardiac lesion is not detected at an early age, lung biopsy may be performed to assess the potential reversibility of pulmonary hypertension after corrective surgery using the Heath and Edwards grading system. Grades I and II represent mild, potentially reversible disease and are characterized by medial hypertrophy, intimal proliferation and the abnormal muscularization of the pulmonary arterioles. Features of intimal laminar fibrosis and progressive vessel obliteration advance the disease to grade III, which is

considered borderline for reversibility. The more severe, largely irreversible grades IV, V and VI contain plexiform lesions, aneurysmal muscular arteries and sites of necrotizing arteritis.

The radiographic features of pulmonary hypertension due to chronic shunt physiology include the familiar complex of prominent central pulmonary arteries and diminished peripheral pulmonary vascularity. Although the right ventricle and atrium typically enlarge in proportion to the volume overload, a normal-sized cardiac silhouette may actually reflect diminished intracardiac shunting due to a markedly elevated pulmonary vascular resistance. Linear calcification and thrombus may be evident in the central pulmonary arteries. In cases of patent ductus arteriosus, mural calcification or aneurysmal dilatation of the ductus may be identified. Significant cardiac volume overload may eventually produce superimposed findings of secondary pulmonary venous hypertension. MR imaging may reveal the septal defect in addition to the characteristic changes of pulmonary hypertension.

Pulmonary embolism may be a complication of deep venous thrombosis, right atrial neoplasia or thrombus, intravenous catheters, or endocarditis of the tricuspid or pulmonic valves. Although acute pulmonary embolism may produce a temporary mild elevation of pulmonary arterial pressure (in 70-80% of cases), verifiably sustained thromboembolic pulmonary hypertension is attributed to chronic, recurrent major vessel pulmonary thromboembolism. An estimated 1-5% of patients with acute pulmonary embolism go on to develop chronic thromboembolic pulmonary hypertension (CTEPH). Pulmonary infarction is a well-documented complication. Clinical onset is insidious and characterized by progressive exertional dyspnea, nonproductive cough, atypical chest pain, tachycardia, syncope and even cor pulmonale. Women are affected more frequently than men. Patients with underlying malignancy, cardiovascular or pulmonary disease are at increased risk. The treatment of choice is surgical thromboendarterectomy (operative mortality 7-40%). Supplemental warfarin anticoagulation therapy is also indicated, in some cases combined with vasodilators, to treat the more peripheral thrombotic occlusions which are beyond the segmental arteries and not amenable to surgical resection. One series has shown that a mean pulmonary artery pressure of 30 mm Hg corresponds to five-year survival in only 30% of patients with CTEPH.

The chest radiograph in CTEPH may be normal or may demonstrate patchy oligemic vascularity. Contrast-enhanced helical CT often provides excellent visualization of emboli in the central pulmonary vessels and segmental arterial branches, and has shown a

greater sensitivity and accuracy for central disease than either pulmonary angiography or MR imaging. HRCT findings also include mosaic lung attenuation accompanied by a marked regional variation in segmental vessels, which can help to distinguish CTEPH from the more diffuse pattern of findings in PPH and other etiologies of pulmonary arterial hypertension. Bronchial artery dilatation and tortuosity were observed on HRCT in 77 % of patients with CTEPH in one series and notably, these findings were statistically significant predictors of patient survival immediately following thromboendarterectomy. Pulmonary angiography maintains greater specificity in the demonstration of central thromboembolic disease than either helical CT or MR imaging, and outlines webs, bands, and stenotic or pouch-like segments which are often confined to one or two lung segments. On T1-weighted MR images, chronic thrombi within the major pulmonary vessels are visualized as discrete, fixed areas of low-to-medium intensity abnormal signal on static systolic spin-echo images which do not change in configuration throughout the cardiac cycle. However, spin-echo MR images demonstrating slow flow in central vessels due to pulmonary hypertension may actually obscure the fixed signal due to central emboli.

Tumor thromboembolism develops in approximately 2-26% of patients with a known solid malignancy, although the diagnosis is frequently missed until postmortem examination. Tumor emboli occlude the small muscular pulmonary arteries and peripheral arterioles, and may coexist with lymphangitic carcinomatosis. Gastric carcinoma is the most common clinically occult neoplasm to embolize and produce pulmonary hypertension. Patients may present with the same constellation of findings as in other causes of pulmonary hypertension. Cor pulmonale in these patients is an ominous sign and often heralds death within 4 to 12 weeks.

Chest radiography may be normal, or may demonstrate enlarged central pulmonary arteries and cardiomegaly compatible with pulmonary arterial hypertension. Ill-defined nodular and confluent peripheral parenchymal opacities are present when multiple pulmonary infarcts have occurred. Radiologic manifestations of lymphadenopathy, pulmonary venous hypertension, and/or lymphangitic carcinomatosis may be evident and suggest the diagnosis of tumor embolism. CT may demonstrate filling defects in the main pulmonary arterial branches, or multifocal beading and dilatation of the peripheral subsegmental pulmonary arteries.

Parasitic embolism is usually attributed to *Schistosoma mansoni* infection, endemic in the Middle East, Africa, the Atlantic coast of South America, and the Caribbean. In humans, Schistosoma eggs may travel

as emboli in the portal-systemic collateral pathways to ultimately lodge in pulmonary muscular arteries and arterioles. The trapped eggs produce an obliterative endarteritis, inciting intravascular and perivascular granuloma formation. Eventually, concentric collagen deposition and fibrosis of pulmonary vessel walls produces clinical pulmonary hypertension, typically in adults aged 25-35 years. Patients present with worsening hepatosplenomegaly, dyspnea, cough, chest pain, cyanosis, and digital clubbing.

In approximately 70% of patients with the clinical manifestations of pulmonary hypertension, chest radiography demonstrates cardiomegaly and central pulmonary arterial enlargement. HRCT of pulmonary schistosomiasis may show nodules, interstitial thickening, and patchy ground-glass attenuation in addition to the typical changes of central arterial and right heart chamber dilatation.

Pulmonary talcosis affects intravenous drug abusers and advances with the chronic, repeated injection of suspensions prepared from crushed tablet compounds. Talc, a common insoluble pharmaceutical binding agent, forms microemboli in the pulmonary circulation and incites a widespread foreign body granulomatous response. Histologic examination of lung tissue reveals scattered granulomas which are packed with doubly refractile talc particles that expand the walls of muscular pulmonary arteries, arterioles, perivascular connective tissue, and the alveolar septa.

Pulmonary talcosis in the early stage manifests radiographically as diffuse, tiny (2-3 mm) well-defined opacities. As the disease advances, conglomerate masses may form in the upper lungs to produce hilar elevation and hyperlucency at the lung bases. On CT there is widespread ground-glass attenuation and scattered fine micronodules. In advanced cases, CT demonstrates lung distortion and confluent perihilar masses which contain high-attenuation areas of accumulated talc.

Clinical Overview: Post-capillary Pulmonary Hypertension

Pulmonary veno-occlusive disease (PVOD) is a rare idiopathic condition and the postcapillary counterpart to PPH. The proposed initial insult in PVOD is patchy or localized venous thrombosis, possibly initiated by infection, toxic exposure or immune complex deposition. PVOD produces distinctive findings of normal or variably elevated capillary wedge pressures. Normal left atrial and left ventricular pressures are characteristic of PVOD and help to exclude cardiac disease as the cause of venous hypertension. One third of PVOD cases occur in children with equal sex distribution, and there is a slight male predominance in adult patients. PVOD may be associated with

pregnancy, bone marrow transplantation, or drug toxicity (BCNU, bleomycin, mitomycin). It is essential for clinicians to distinguish PVOD from pre-capillary pulmonary hypertension, because potentially fatal pulmonary edema may be induced by the administration of vasodilator therapy for presumed pulmonary arterial hypertension. While treatment with anticoagulants has had limited success in PVOD, this disease is usually fatal within three years of diagnosis.

The diagnosis of PVOD is suggested radiographically when features of pulmonary arterial hypertension are accompanied by evidence of diffuse pulmonary interstitial edema and a normal-sized left atrium. CT in PVOD may demonstrate features of secondary pulmonary arterial hypertension in addition to distinctive findings of markedly small central pulmonary veins, central and gravity-dependent ground-glass lung attenuation, smoothly thickened interlobular septa, pleural effusions, a normal-sized left atrium, and centrilobular nodules. Pulmonary angiography in PVOD shows enlarged central pulmonary arteries, dilated right ventricle, prolonged parenchymal phase enhancement, delayed filling of normal pulmonary veins, and the outline of a normal to small left atrium.

Left-sided cardiac disease is the most common etiology of pulmonary venous hypertension, and underlying conditions include left ventricular failure, left atrial thrombus or neoplasia (myxoma, sarcoma, metastasis), mitral stenosis and congenital cardiac anomalies. Patients with left atrial myxoma commonly present with dyspnea, tachyarrhythmias, and pulmonary venous hypertension due to interference with either pulmonary venous drainage or mitral valve function. Both obstructive left atrial myxoma and severe mitral stenosis have been shown to produce an abnormal systolic reversal of the pulmonary venous flow (measured by transesophageal and transthoracic Doppler echocardiography, and phase-shift MR) due to retrograde transmission of an elevated left atrial pressure throughout the cardiac cycle. These findings illustrate the underlying hemodynamics which may lead to the development of pulmonary venous hypertension in left-sided cardiac lesions.

Left-sided cardiac disease may mimic PVOD radiographically with features of pulmonary interstitial edema, Kerley B lines, pleural effusions, and secondary central pulmonary arterial prominence. However, the presence of left atrial enlargement can distinguish left-sided cardiac lesions, such as mitral stenosis, from PVOD. Hemosiderosis due to longstanding pulmonary venous hypertension produces fine reticular opacities on chest radiographs, and tiny (1-3 mm) calcified ossific nodules are the hallmark of mitral stenosis. Rarely, a left atrial myxoma manifests as a

heavily calcified mass. Angiography has been replaced by echocardiography in the evaluation of intracardiac lesions to delineate the size, configuration, mobility, attachment site, and relationship to the atrioventricular valve. CT often complements echocardiography by demonstrating an intracardiac soft tissue mass with additional evidence of extracardiac extension, interstitial edema, vascular congestion, pleural effusions, and enlargement of central vessels due to secondary pulmonary arterial hypertension.

Mediastinal fibrosis is a progressive proliferation of fibrous tissue and collagen in the mediastinum attributed to various causes, most importantly prior granulomatous (especially *Histoplasma capsulatum* and tuberculosis) infection. It may constrict or completely occlude vital mediastinal structures including the superior vena cava, central airways, esophagus, pericardium, central pulmonary arteries and draining pulmonary veins. Pulmonary vascular occlusion is produced by fibrous encasement of the pulmonary arteries and/or veins in a non-uniform pattern. The clinical presentation of dyspnea, hemoptysis, and signs of pulmonary arterial involvement by mediastinal fibrosis is often mistaken for chronic large vessel thromboembolic disease. Surgical resection of the fibrotic tissue has been effective in focal pulmonary venous obstruction; steroid therapy has met with limited success.

Radiographic features consistent with the diagnosis of mediastinal fibrosis (producing pulmonary venous constriction) include asymmetric mediastinal widening and/or a hilar mass with calcifications accompanied by ipsilateral Kerley B lines. CT may reveal mediastinal and hilar nodal masses of soft tissue attenuation containing coarse calcifications, which helps to distinguish mediastinal fibrosis from unilateral chronic thromboembolism. An area of venous infarction may be visualized as a peripheral wedge-shaped consolidation on CT. Pulmonary angiography may show unilateral or asymmetric narrowing of central pulmonary arteries and distal arterial cut-offs when mediastinal fibrosis affects the arterial side of the pulmonary circulation; with involvement of pulmonary veins, the venous phase shows non-uniform pulmonary vein obstruction, stenosis or focal dilatation near the left atrium.

Summary

Pre-capillary pulmonary hypertension affects the arterial side of the pulmonary circulation, chiefly at the level of the muscular arteries. The marked hemodynamic changes of elevated pulmonary arterial pressure and high vascular resistance are associated with histologic findings of medial hypertrophy, intimal cellular proliferation, thrombosis, and in certain conditions,

“plexiform” lesions. Diseases implicated in the development of pre-capillary pulmonary hypertension include idiopathic primary pulmonary hypertension, sustained cardiac left-to-right shunt, chronic interstitial lung disease, chronic thromboembolic disease, and pulmonary emboli arising from tumor cells, parasitic organisms, or talc particles.

The radiologic manifestations of pre-capillary pulmonary hypertension reflect central pulmonary arterial enlargement with sharply diminished peripheral vascularity, mosaic perfusion, and right heart hypertrophy and chamber dilatation. Findings are characteristically diffuse in distribution with the exception of chronic thromboembolic disease, which may be limited to a few segmental or subsegmental vessels. Pulmonary infarcts, calcified plaques of the larger pulmonary arteries, and dissection or massive thrombosis of the central pulmonary arteries are complications which may be evident radiologically. Certain radiologic findings are helpful in distinguishing the causes of pre-capillary pulmonary hypertension and pulmonary infarction. Coexistent lymphangitic carcinomatosis suggests tumor embolism as the underlying mechanism. Hepatosplenomegaly is associated with cardiopulmonary schistosomiasis. Pulmonary talcosis manifests with distinctive micronodular opacities and diffuse ground-glass attenuation, which may eventually converge into perihilar fibrotic masses containing high density material.

Post-capillary pulmonary hypertension affects the venous side of the pulmonary circulation and produces either a uniform or widely variable elevation of pulmonary capillary wedge pressures. The hemodynamic derangements of precapillary pulmonary hypertension also may be present when the elevated pulmonary venous pressure is transmitted retrograde across the capillary bed. The histologic changes include venous medial hypertrophy and intimal proliferation, thickening of the venous internal elastic lamina, capillary congestion and proliferation, interlobular septal thickening, lymphatic dilatation, and occasionally venous infarction. Etiologies include pulmonary veno-occlusive disease (diagnosed by unique microscopic findings of recanalized thrombosis within the pulmonary veins), left-sided cardiac lesions which compromise pulmonary venous drainage, and extrinsic lesions compressing the pulmonary veins such as mediastinal fibrosis.

The radiology of post-capillary pulmonary hypertension typically demonstrates features of pulmonary interstitial edema, often accompanied by findings of

pre-capillary pulmonary hypertension. Prominent central pulmonary arteries, Kerley B lines, thickened pleural fissures and small effusions are characteristic findings which may be accompanied by a wedge-shaped consolidation when macroscopic venous infarction is present. The CT features which suggest PVOD are marked narrowing of the central pulmonary veins and a normal-sized left atrium. A left atrial mass obstructing pulmonary venous outflow is often revealed by echocardiography or contrast-enhanced chest CT. Remarkable left atrial enlargement in post-capillary pulmonary hypertension suggests severe underlying mitral stenosis. Mediastinal fibrosis is distinguished by a soft tissue mediastinal or hilar mass containing coarse calcifications, accompanied by a regional distribution of Kerley B lines.

REFERENCES

1. Burke A, Virmani R. Mini-symposium: Pulmonary pathology: Evaluation of pulmonary hypertension in biopsies of the lung. *Current Diagnostic Pathology* 1996;3:14-26.
2. Edwards WD. Pathology of pulmonary hypertension. In: Brest AN, editor. *Cardiovascular Clinics*. Philadelphia: F.A. Davis Company, 1988; 321-359.
3. Burke AP, Farb A, Virmani R. The pathology of primary pulmonary hypertension. *Mod Pathol* 1991;4(2):269-82.
4. Sherrick AD, Swensen SJ, Hartman TE. Mosaic pattern of lung attenuation on CT scans: frequency among patients with pulmonary artery hypertension of different causes. *AJR Am J Roentgenol* 1997;169(1):79-82.
5. Bergin CJ, Rios G, King MA, Belezzuoli E, Luna J, Auger WR. Accuracy of high-resolution CT in identifying chronic pulmonary thromboembolic disease. *AJR Am J Roentgenol* 1996;166(6):1371-7.
6. White RD, Higgins CB. Magnetic resonance imaging of thoracic vascular disease. *J Thorac Imaging* 1989;4(2):34-50.
7. Bergin CJ, Sirlin CB, Hauschildt JP, Huynh TV, Auger WR, Fedullo PF, et al. Chronic thromboembolism: Diagnosis with helical CT and MR imaging with angiographic and surgical correlation. *Radiology* 1997;204:695-702.
8. Remy-Jardin M, Remy J, Watinne L, Giraud F. Central pulmonary thromboembolism: diagnosis with spiral volumetric CT with the single-breath-hold technique—comparison with pulmonary angiography. *Radiology* 1992;185(2):381-7.
9. Shepard JA, Moore EH, Templeton PA, McLoud TC. Pulmonary intravascular tumor emboli: dilated and beaded peripheral pulmonary arteries at CT [see comments]. *Radiology* 1993;187(3):797-801. 1984; 64(2):281-4.
10. Maltby JD, Gouverne ML. CT findings in pulmonary venoocclusive disease. *J Comput Assist Tomogr* 1984;8(4):758-61.

Helical CT for Pulmonary Embolism: Current Status

Ella A. Kazerooni, MD

At the time of publication, no abstract was available.

Disclosure Statement: GEMS-CT Medical Advisory Board.

Information Management: PACS, Patient Data, and Diagnosis

Paul J. Chang, MD

At the time of publication, no abstract was available.

Disclosure Statement: founder, Stentor, Inc.; medical advisory panels, Agfa, IDX; contracts/
grants: NIH, DARPA, NLM.
